Bcl-xL Enforces a Slow-Cycling State Necessary for Survival in the Nutrient-Deprived Microenvironment of Pancreatic Cancer
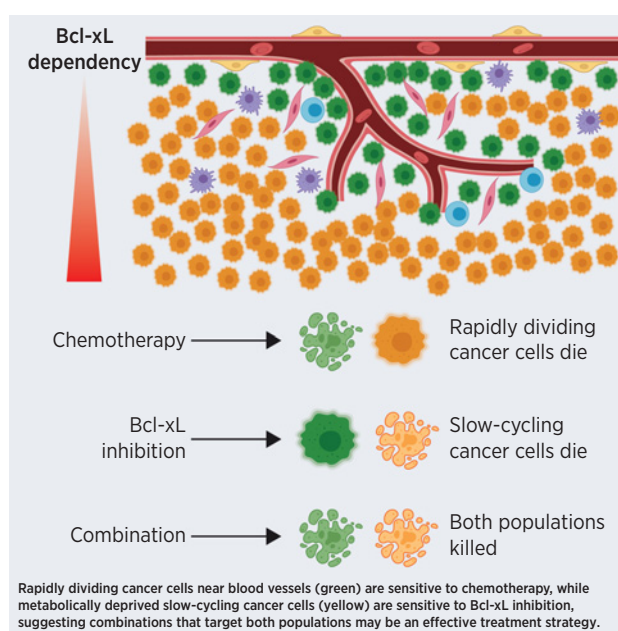
Yogev Sela[1,2], Jinyang Li[1,2], Shivahamy Maheswaran[1,2], Robert Norgard[1,2], Salina Yuan[1,2], Maimon Hubbi[1,2], Miriam Doepner[1], Jimmy P. Xu[3], Elaine S. Ho[3], Clementina Mesaros[3], Colin Sheehan[4], Grace Croley[4], Alexander Muir[4], Ian A. Blair[3], Ophir Shalem[5,6], Chi V. Dang[7,8], and Ben Z. Stanger[1,2]

ABSTRACT

Solid tumors possess heterogeneous metabolic microenvironments where oxygen and nutrient availability are plentiful (fertile regions) or scarce (arid regions). While cancer cells residing in fertile regions proliferate rapidly, most cancer cells *in vivo* reside in arid regions and exhibit a slow-cycling state that renders them chemoresistant. Here, we developed an *in vitro* system enabling systematic comparison between these populations via transcriptome analysis, metabolomic profiling, and whole-genome CRISPR screening. Metabolic deprivation led to pronounced transcriptional and metabolic reprogramming, resulting in decreased anabolic activities and distinct vulnerabilities. Reductions in anabolic, energy-consuming activities, particularly cell proliferation, were not simply byproducts of the metabolic challenge, but rather essential adaptations. Mechanistically, Bcl-xL played a central role in the adaptation to nutrient and oxygen deprivation. In this setting, Bcl-xL protected quiescent cells from the lethal effects of cell-cycle entry in the absence of adequate nutrients. Moreover, inhibition of Bcl-xL combined with traditional chemotherapy had a synergistic antitumor effect that targeted cycling cells. Bcl-xL expression was strongly associated with poor patient survival despite being confined to the slow-cycling fraction of human pancreatic cancer cells. These findings provide a rationale for combining traditional cancer therapies that target rapidly cycling cells with those that target quiescent, chemoresistant cells associated with nutrient and oxygen deprivation.

for their survival, providing a compelling antitumor metabolic strategy.

Significance: The majority of pancreatic cancer cells inhabit nutrient- and oxygen-poor tumor regions and require Bcl-xL

Rapidly dividing cancer cells near blood vessels (green) are sensitive to chemotherapy, while metabolically deprived slow-cycling cancer cells (yellow) are sensitive to Bcl-xL inhibition, suggesting combinations that target both populations may be an effective treatment strategy.

Introduction

Uncontrolled proliferation is a hallmark of cancer, and thus most existing therapeutic strategies have been designed to target rapidly cycling cancer cells. However, the majority of cancer cells in solid tumors do not proliferate at any given time (1, 2). The biology of these slow-cycling cancer cells is poorly characterized and rarely modeled despite the strong correlation between quiescence and therapy resistance (3, 4). Filling this knowledge gap is critical, as a

[1]Departments of Medicine and Cell and Developmental Biology, Perelman School of Medicine, University of Pennsylvania, Philadelphia, Pennsylvania. [2]Abramson Family Cancer Research Institute, Perelman School of Medicine, University of Pennsylvania, Philadelphia, Pennsylvania. [3]Department of Systems Pharmacology and Translational Therapeutics, Perelman School of Medicine, University of Pennsylvania, Philadelphia, Pennsylvania. [4]Ben May Department of Cancer Research, University of Chicago, Chicago, Illinois. [5]Center for Cellular and Molecular Therapeutics, Children's Hospital of Philadelphia, Philadelphia, Pennsylvania. [6]Department of Genetics, Perelman School of Medicine, University of Pennsylvania, Philadelphia, Pennsylvania. [7]Systems and Computational Biology Center and Molecular and Cellular Oncogenesis Program, The Wistar Institute, Philadelphia, Pennsylvania. [8]Ludwig Institute for Cancer Research, New York, New York.

Corresponding Author: Ben Z. Stanger, Perelman School of Medicine, University of Pennsylvania, 421 Curie Bouelvard, Philadelphia, PA 19104. Phone: 215-746-5560; E-mail: bstanger@upenn.edu

AACR American Association for Cancer Research

better understanding of the slow-cycling population of cancer cells could reveal new therapeutic opportunities, including drugs that could complement existing treatments.

The spatial distribution of rapidly and slowly cycling cells in solid tumors is not uniform. Rather, cancer cells exist in a continuum of metabolic microenvironments based on their proximity to patent blood vessels and nutrient access: a proximal (well-perfused) zone enriched for rapidly cycling tumor cells, an intermediate (poorly perfused) zone dominated by viable slow-cycling cells, and a distal (nonperfused) zone with high levels of necrosis (5–7). Such metabolic zonation, characterized by varying levels of blood-borne nutrients and growth factors, likely dictate the proliferative and biosynthetic state of cancer cells (2, 8, 9).

Existing models of nutrient deprivation use cell culture conditions with a reduced abundance of specific nutrients including glucose, amino acids, growth factors, and oxygen (10, 11), enabling the application of genetic screening (12–16). Whereas these studies have identified dependencies resulting from the absence of single or paired nutrients, cancer cells in poorly perfused regions of a tumor most likely suffer from the simultaneous deprivation of many nutrients and oxygen. This distinction is important because tumor cells deprived of one nutrient can possibly survive through the utilization of other compensating metabolic pathways. Moreover, cells grown under most previously reported conditions continued to proliferate and thus do not fully model the slow-cycling and chemoresistant population.

Here, we established an *in vitro* experimental system to model the nutrient- and oxygen-deprived metabolic microenvironments of pancreatic tumors to understand how cancer cells adapt to comprehensive metabolic deficits. Through unbiased genetic screening, molecular profiling, and functional validation, we have identified vulnerabilities specific to metabolically deprived slow-cycling cancer cells and associated therapeutic opportunities.

Materials and Methods

Cell culture

Human pancreatic and colorectal cancer cell lines were obtained from Anil Rustgi (University of Pennsylvania, Philadelphia, PA). MDA-MB-231 breast cancer cells were obtained from Andy Minn (University of Pennsylvania). Mouse MH6620c1 were previously isolated from late-stage primary tumors in C57BL/6 KPCY mice and generated by limiting dilution as described (17) and tested by the Research Animal Diagnostic Laboratory (RADIL) at the University of Missouri (Columbia, MO), using the Infectious Microbe PCR Amplification Test (IMPACT) II. Cultures were regularly tested using the MycoAlert Mycoplasma Detection Kit (Lonza). Tumor cells were cultured under "fertile" or "arid" conditions using the following conditions:

Fertile conditions

DMEM (high glucose without sodium pyruvate) with 10% FBS (Gibco), glutamine (2 mmol/L), and penicillin/streptomycin (1%) in 20% oxygen. Cells were passaged when 70%–80% confluent.

Arid conditions

Basal media was prepared by dissolving 11 g of DMEM without amino acids/glucose/pyruvic acid (D9800-26, US Biological) into 1 L of distilled water (WFI grade) pH adjusted to 7.0–7.1. Basal media were mixed with DMEM containing amino acids without glucose/sodium pyruvate (Gibco) at a 1:4 ratio (to 20%) to which 0.5% FBS (Gibco) 2.5 mmol/L glucose, 25 mmol/L HEPES (Gibco)

1% penicillin/streptomycin (Gibco), 0.2% nonessential amino acids (Gibco), and 0.4 mmol/L glutamine (Gibco) were added. Cells were plated at 37,500 cells/cm² in all arid experiments and cultured under 1% oxygen (Heracell 150i Thermo) with daily media replacement and without passaging.

Flow cytometry
Assessment of viability

For assessment of viability, media were collected from culture before harvest and combined with the pellet of the cells dissociated by trypsin. Cells were washed with PBS and Annexin staining buffer, stained with Annexin-V-APC (eBioscience) for 15 minutes, washed and incubated with propidium iodide (PI) or DAPI as specified in each experiment.

EdU and OPP labeling *in vitro*

Tumor cells were pulsed with 10 μmol/L EdU 24 hours before endpoint or 50 μmol/L OPP 1 hour before endpoint, followed by trypsinization, staining with Live/Dead Fixable Aqua Stain Kit (Thermo) and fixation with the FoxP3 Transcription Factor Staining Buffer Set (eBioscience). Cells were then stained using the Click-iT reaction solution (100 mmol/L Tris-HCl pH 8.5, 4 mmol/L CuSO₄, 100 mmol/L ascorbic acid) for 30 minutes at room temperature and analyzed by flow cytometry.

PKH proliferation kinetics assay

Tumor cells were trypsinized and stained with PKH26 (Sigma) or PKH67 (Sigma) according to the manufacturer's protocol. Briefly, cells were stained with dye for 3 minutes, washed with serum, and seeded under fertile conditions. Tumor cells were sampled 24 hours later (t0) and cells were then cultured under fertile or arid conditions for 14–21 days depending on the experiment. Tumor cells were stained with DAPI and analyzed by flow cytometry at various time points to derive population doubling times.

Competition assays

Competition assays were performed by mixing EV cells and genetically modified cells at 1:1 ratio. Cells were sampled at day 0 by FACS to account for initial distributions and all subsequent measurements were normalized to day 0. For competition assays starting under arid conditions, PANC1 cells expressing Cas9 were transduced with sgBcl-xL-mCherry or nontargeting-mCherry vectors at a precalculated titer such that approximately 50% of the cells were transduced as determined by mCherry expression at day 4 posttransduction by flow cytometry.

Pharmacologic studies *in vitro*

For drug sensitivity assays, cells in the fertile culture were seeded on 12-well dishes at 18,000 cells/cm² and treated with selected drugs 24 hours later. The arid group was cultured for 0 (acute arid) or 14 (chronic arid) days under arid conditions prior to drug treatment. Cells supplemented daily for 4–5 days with fresh media supplemented with various drugs including: gemcitabine (Pfizer), PHA-767491 (Cayman Chemical), Silvestrol (Biovision), CPI-613 (Cayman Chemical), UK 5099 (Cayman Chemical) or A-1155463 (Cayman Chemical), or vehicle (0.2% DMSO). Tumor cells were fixed at day 0 or endpoint (day 4–5) with paraformaldehyde 4% stained with 3 μmol/L Hoecsht 33342 (Thermo Fisher Scientific) for 30′ at 37°C and quantified using a fluorescence plate reader (Molecular Devices) to assess cell numbers. Cell density was normalized for day 0 of each group.

For pharmacologic inhibition of biosynthesis under serum reple-tion, treatment initiated with switch to arid conditions (acute arid) and cells were treated for 72 hours before readouts. Drugs used in that study include: Abemaciclib (MedChem Express), rapamycin (ApexBio), Torin1 (MedChem Express), and cycloheximide (Sigma).

CRISPR-Cas9 screen

Cas9 was introduced to the PANC1 cell line by transduction of the lentiCas9-Puro construct (Addgene plasmid #52962), and selected with 10 μg/mL blasticidin. 320 million Cas9-expressing cells were transduced with the Brunello sgRNA library (18) at a MOI of 0.3 such that approximately 30% of cells were puromycin resistant yielding $300\times$ coverage of the sgRNA library. T0 samples were collected by FACS 3 days posttransduction. Cells were selected under fertile conditions in the presence of puromycin 2 μg/mL for additional 5 days to achieve complete puromycin selection and cultures were separated for culture under fertile or arid conditions as described above (see Results section). Genomic DNA from half of the cell pellets representing $150\times$ coverage was processed for library generation. DNA was extracted by incubation with NK lysis Buffer (50 mmol/L Tris, 50 mmol/L EDTA, 1% SDS, pH 8) and 20 mg/mL Proteinase K (Qiagen 19131) at 55°C overnight, followed by incu-bation with 10 mg/mL RNAse A (Qiagen 19101) at 37°C for 30 minutes and protein precipitation using 7.5 mol/L ammonium acetate (Sigma A1542). Precipitate was vortexed and then centri-fuged at $\geq 4{,}000 \times g$ for 10 minutes, washed with 100% isopropanol, and 70% ethanol and the pellet was air dried and resuspended in $1\times$ TE buffer (Sigma T9285).Libraries were constructed according to previously described protocols (19). Briefly, sgRNAs were amplified over 24 cycles with Herculase II fusion DNA polymerase (Agilent) as per manufacturer's specifications with PCR#1 forward and reverse primers. Each reaction included 5 μg of genomic DNA, and multiple PCR reactions were run in parallel such that all extracted genomic DNA was used to maintain library coverage. PCR reactions were then pooled for each sample, and 5 μL of each pooled PCR#1 sample was used as a template for PCR#2, which added Illumina P5/P7 adapters, barcodes, and staggers for nucleotide complexity. For PCR#2, template was amplified over 7 cycles with PCR#2 forward and reverse primers, and the resulting reactants were column purified with the QIAquick PCR Purification Kit (Qiagen) and gel extracted with the QIAquick Gel Extraction Kit (Qiagen). The barcoded libraries were then pooled at an equal molar ratio and sequenced on a NextSeq500/550 sequencer (Illumina, 150 cycles High Output kit v2.0) to generate 150-bp single-end reads. MAGeCK software was used for analysis. Briefly, the resulted sequencing data were debarcoded, merged, and the 20 bp sgRNA sequence was aligned to the reference sgRNA library without allowing for any mismatches. The read counts were calculated for each sgRNA with normalization to the nontargeting sgRNAs. Differential analysis of sgRNA and targeted genes was done following the MAGeCK pipeline with standard parameters. Pathway analysis of identified genes were done using EnrichR (https://maayanlab.cloud/Enrichr/). Detailed scripts and parameters used for each step of analysis could be provided by request to the authors.

Table 1. Primers used for library preparation.

PCR #1 forward	AATGGACTATCATATGCTTACCGTAACTTGAAAGTATT TCG
PCR #1 reverse	CTTTAGTTTGTATGTCTGTTGCTATTATGTCTACTATTCT TTCC

Table 2. Stagger sequence and barcode sequence.

Sample	PCR #2 forward primer sequence
d0	AATGATACGGCGACCACCGAGATCTACACTCTTTCCCTACA CGACGCTCTTCCGATCT*ACGATCGAT***TCCTTGGT**TCTTGTG GAAAGGACGAAAC-ACCG
d9 fertile	AATGATACGGCGACCACCGAGATCTACACTCTTTCCCTACA CGACGCTCTTCCGATCT*T***ACAGGTAT**TCTTGTGGAAAGG ACGAAACACCG
d30 arid	AATGATACGGCGACCACCGAGATCTACACTCTTTCCCTACA CGACGCTCTTCCGATCT*AT***CTAACTCG**TCTTGTGGAAAGG ACGAAACACCG
d30 fertile	AATGATACGGCGACCACCGAGATCTACACTCTTTCCCTACA CGACGCTCTTCCGATCT*GAT***AACAATGG**TCTTGTGGAAA GGACGAAACACCG
d32 fertile	AATGATACGGCGACCACCGAGATCTACACTCTTTCCCTACA CGACGCTCTTCCGATCT*CGAT***ACTGTATC**TCTTGTGGAA AGGACGAAACACCG
d53 arid	AATGATACGGCGACCACCGAGATCTACACTCTTTCCCTACA CGACGCTCTTCCGATCT*TCGAT***AGGTCGCA**TCTTGTGGA AAGGACG-AAACACCG
d53 fertile	AATGATACGGCGACCACCGAGATCTACACTCTTTCCCTACA CGACGCTCTTCCGATCT*CGATCGAT***CCAACATT**TCTTGTG GAAAGGACGAAACACCG

PCR #2 reverse primer sequence

CAAGCAGAAGACGGCATACGAGATGTGACTGGAGTTCAGACGTGTGCTC TTCCGATCTTCTACTATTCTTTCCCCTGCACTGT

Note: Stagger sequence is denoted by italic font and barcode sequence is denoted by bold font.

See **Table 1** for primers used for library preparation. For stagger sequence and barcode sequence, see **Table 2**. Processed read counts from the CRISPR screen are presented in Supplementary Table S1.

RNA-seq analysis

RNA samples were extracted using the Qiagen RNeasy Kit, follow-ing manufacturer's instructions. RNA samples were sent for library preparation and next generation sequencing by Novogene. Raw counts of gene transcripts were derived from fastq files using an alignment-independent quantification tool, Salmon (https://combine-lab.github. io/salmon/), with standard settings. The raw count matrix was then imported into R-studio and utilized as input for DESeq2 analysis for normalization, differential gene expression analysis, and principal component analysis. The output of DESeq2 was used as the input for preranked based GSEA for enrichment of functional pathways and gene signatures (https://www.gsea-msigdb.org/gsea/index.jsp). Detailed scripts and parameters used for each step of analysis can be provided by the authors upon request.

Expression analysis and overall survival analysis in human samples

Analysis of the expression of *BCL2L1* across different types of cancer and normal tissues, and correlation with overall survival, was done using an online tool, Gene Expression Profiling Interactive Analysis (GEPIA; http://gepia.cancer-pku.cn/). Analysis of the expression of *BCL2L1* in proliferating and quiescent cancer cells using published single-cell RNA-seq datasets of human pancreatic cancer samples was done using Seurat (https://satijalab.org/seurat/). The output of Seurat-based differential gene expression analysis was used as the input for preranked based GSEA for enrichment of functional pathways

and gene signatures (https://www.gsea-msigdb.org/gsea/index.jsp). Detailed Scripts and parameters used for each step of analysis can be provided by the authors upon request.

Metabolomics

Metabolomic extraction

Metabolomic extraction from cells was done as described previously (20). 1 mL of cold 80% MeOH from −80°C and 40 μL of Metabolomics ISTD mix were added to each plate (Supplementary Table S2). Cells were scraped and transferred to microcentrifuge tubes in ice. Samples were pulse-sonicated in ice with a sonic dismembranator (Thermo Fisher Scientific) for 30 seconds, incubated on ice for 10 minutes, and then pulsed again for 30 seconds. Samples were pelleted by centrifugation at $6,000 \times g$ for 5 minutes at room temperature. Five-hundred microliters of supernatant was moved to a clean microcentrifuge tube, dried under nitrogen, and resuspended in 50 μL of 5% (w/v) SSA in water. Three-microliter injections were used for LC-HRMS analysis.

Metabolomic LC-HRMS

Metabolites were separated using a XSelect HSS C18 column (2.1 mm × 150 mm, 3.5 μm particle size; Waters) in an UltiMate 3000 quaternary UHPLC (Thermo Scientific) equipped with a refrigerated autosampler (5°C) and column heater (50°C). Solvent A consisted of water with 5 mmol/L DIPEA and 200 mmol/L HFIP and Solvent B consisted of MeOH with 5 mmol/L DIPEA, and 200 mmol/L HFIP. Flow gradient conditions were as follows: 0% B for 6 minutes at 0.18 mL/minute, increased to 1% B for 2 minutes at 0.2 mL/minute, increased to 2% B for 4 minutes, increased to 14% B for 2 minutes, increased to 70% B for 2 minutes, increased to 99% B for 1 minutes, increased flow rate to 0.3 mL/minute for 0.5 minutes, increased flow rate to 0.4 mL/minute for 4 minutes, then washed by decreasing to 0% B for 2.3 minutes at 0.3 mL/minute, decreased to 0.2 mL/minute for 0.2 minutes, and ending with flow of 0.18 mL/minute. Samples were analyzed using a Q Exactive HF (QE-HF; Thermo Scientific) equipped with a heated electro-spray ionization (HESI) source operated in the negative ion mode as described by Frederick and colleagues Column effluent was diverted to the QE-HF from 0.5 to 19 minutes and then to waste for the remaining time of the run.

Timelapse microscopy

PANC1 WT and Bcl-xL KO cells tagged with the FUCCI-PIP reporter (Addgene #138715; ref. 21), were seeded on 12-well plates (BD Falcon), cultured under arid conditions for 48 hours and imaged for additional 48 hours hours via EVOS Auto FL2 microscope (Thermo Fisher Scientific) under 1% or 20% oxygen and images acquired hourly. Timelapse movies were constructed via ImageJ and quantification of cell-cycle transitions and cell death was done manually.

ATP measurements

For ATP measurements, 10,000 tumor cells were seeded in parallel on standard (for cell numbers) or opaque (for ATP) 96-well plates and cultured under fertile or arid condition for 3 or 14 days. ATP was then assessed using CellTiter-Glo (Promega) and cell numbers were quantified by Hoechst 33342 staining as described above to derive ATP/cell ratios.

Western blots

Cells were washed with ice-cold PBS and lysed in RIPA buffer (Cell Signaling Technology). Equal amounts of protein were run in reducing conditions on 4%–20% Mini-PROTEAN gels (Bio-Rad) and transferred to Immun-Blot PVDF Membrane (Bio-Rad). Blocking was performed in 5% nonfat dry milk for 1 hour at room temperature. After blocking, membranes were incubated in primary antibody diluted in 5% nonfat dry milk overnight at 4°C. After PBS-T washes, membranes were incubated with secondary antibody diluted in 5% nonfat dry milk at room temperature for 1 hour. Following PBS-T washes, membranes were soaked in ECL or ECL plus (Pierce) kits depending on the target and imaged with Chemi-doc imaging system (Bio-Rad). The following antibodies were used: monoclonal mouse S6 1:1,000 (Cell Signaling Technology, 2317S), polyclonal rabbit phospho S6 ribosomal protein (Ser235/236) 1:1,000 (Cell Signaling Technology 2211S), monoclonal mouse α-tubulin 1:5,000 (Cell Signaling Technology 3873S, c-myc, rabbit polyclonal Bcl-xL 1:1,000 (ProteinTech 10783–1-AP), rabbit polyclonal 1:1,000 Mcl-1 (ProteinTech 16225–1-AP).

Immunofluorescence and microscopy

Tissue processing and IHC

Tumors were fixed by 4% paraformaldehyde for 24 hours, followed by incubation in 30% sucrose for 24 hours, embedding in optimal cutting temperature, and freezing on dry ice. Frozen sections (7 μm) were obtained using a cryostat (Leica) and stored at −80°C. For staining, sections were thawed, blocked in 0.3% Triton-X with 5% normal donkey serum for 1 hour, incubated overnight with rat monoclonal Ki-67 (eBioscience, 1:100), rabbit polyclonal cleaved caspase-3 (CC3) antibody (Cell Signaling Technology,1:200), rabbit G0S (ProteinTech 1:100), rabbit FABP5 (ProteinTech 1:100), or rabbit UPAR (ProteinTech 1:400) in 5% donkey serum in PBST 0.1%. Sections were then washed, incubated with secondary antibodies and DAPI for 1 hour, and mounted. For EdU staining, samples were permeabilized with 0.5% Triton-X for 20 minutes, washed and incubated with buffer containing 100 mmol/L Tris-HCl pH 8.5, 8 mmol/L $CuSO_4$, and 100 mmol/L ascorbic acid for 30 minutes at room temperature followed by immunostaining as described. Whole-tumor sections were visualized using a LSM710 equipped with an ×20 objective and robotic stage. Images were quantified using ImageJ. To calculate distance from perfused blood vessels, dextran pixels were thresholded to create a 32-bit EDM map. For each analysis, pixels of choice (e.g., GFP[+], mCherry[+], GFP[+]CC[+] pixels, etc.) were thresholded and overlaid on EDM maps to derive spatial histograms of each type of pixel. Percentages of Ki-67^{+} and CC3^{+} pixels in tumor cells was defined as the ratio of colocalizing pixels (Ki-67 or CC3)/total tumor pixels derived from spatial histograms.

Immunocytochemistry

Tumor cells were fixed with 4% paraformaldehyde for 15 minutes, blocked with 5% donkey serum for 1 hour and stained overnight at 4°C with Ki-67 (eBioscience, 1:100), or rabbit polyclonal phospho-S6 (Cell Signaling Technology, 1:400) in 5% donkey serum in PBST 0.1%, stained with secondary antibody and DAPI and imaged by EVOS Auto FL2 Microscope (Thermo Fisher)

Lentivirus transduction of tumor cells for CRISPR-mediated ablation

Cell lines were first transduced with Lentspicas9-puro (Addgene plasmid #108100; ref. 22) or Lenti-v2-Cas9-GFP (Addgene plasmid #82416; ref. 23). sgRNAs were cloned into LRGFP (Addgene plasmid #65656; ref. 24) or LRmCherry (a gift from Shi Junwei, University of Pennsylvania). Tumor cells modified to expressed

Table 3. Primer sequences from which sgRNAs were derived.

Target gene	Forward primer	Reverse primer
Human TSC2-1	caccgCAGCATCT CATACACACGCG	aaacCGCGTGTGTA TGAGATGCTGc
Human TSC2-2	caccgCCTCTACAGG AACTTTGCCG	aaacCGGCAAAGTT CCTGTAGAGGc
Human Bcl-xL1	caccgCAGGCGACGA GTTTGAACTG	aaacCAGTTCAAACT CGTCGCCTGc
Human Bcl-xL2	caccgGACCCCAGTT TACCCCATCC	aaacGGATGGGG TAAACTGGGGTCc
Mouse Bcl-xL	caccgAGTAAACT GGGGTCGCATCG	aaacCACATGTGTG CTAGGATCAGc
Nontargeting	caccgGCTTGAGC ACATACGCGAAT	aaacATTCGCGTA TGTGCTCAAGCc

spCas9 were transduced with sgRNAs derived from the primer sequences given in **Table 3**.

All lentiviral and retroviral vectors were transfected into 293T cells using 1 mg/mL PEI, and virus was harvested 48 hours and 72 hours later. Viral particles were transduced into cells using 4 µg/mL polybrene.

Autophagy

PANC1 cells were transduced with a pBABE-puro mCherry-EGFP-L3CB (Addgene plasmid #22418; ref. 25). At day 14, tumor cells were analyzed by flow cytometry and the ratio of mCherry/GFP fluorescence was measured.

Macropinocytosis

PANC1 cells were seeded onto glass coverslips and grown under fertile conditions for 24 hours or arid conditions for 14 days. Media was then switched to arid media containing 1 mg/mL TMR-dextran (D1818, Invitrogen) for 30 minutes at 37°C. At the end of the incubation period, cells were rinsed five times in cold PBS and immediately fixed in 3.7% formaldehyde. Cells were DAPI-treated to stain nuclei and coverslips mounted onto slides using Aquamount (Thermo). Images ($\times$63 oil lens, 0.7-µm optical sections) were captured by confocal microscopy using a LSM880 (Zeiss) and analyzed using the "Analyze Particles" feature in ImageJ (NIH, Bethesda, MD). Three fields were analyzed for each experimental group in each experiment.

Animal studies

Kras$^{LSL-G12D}$; p53$^{L/+}$; Pdx1-cre; Rosa26$^{YFP/YFP}$ (KPCY) mice have been described previously. Six- to 8-week-old C57BL/6J (male) or NOD.SCID (male and female) mice were purchased from The Jackson Laboratories and Charles River Laboratories, respectively, for tumor cell injection experiments. All vertebrate animal experiments were conducted in compliance with the NIH guidelines for animal research and approved by the University of Pennsylvania Institutional Animal Care and Use Committee.

Evaluation of proliferation in differentially perfused regions

To estimate proliferation and cell death in differentially perfused regions, mice bearing KPCY tumors ($\sim$10 mm in diameter) were injected four times with 10 mg/kg EdU over a period of 48 hours in 12-hour intervals. Mice were injected with 70 kDa TMR-dextran (Invitrogen) 30 minutes prior to sacrifice and two different sections per mouse, 5 well perfused, and 5 poorly perfused regions were evaluated for proliferation and apoptotic markers by manual counting of YFP$^+$ cells.

Establishment and evaluation of tumor xenografts

Cells containing EV-GFP and Bcl-xL KO-mCherry clones 8×10^6 cells in DMEM were inoculated into the flanks of NOD.SCID mice (males and females) and tumor size was measured by calipers starting 6 weeks postimplantation. Proliferation and cell death were measured in two separate sections per mouse.

Competition assay *in vivo*

EV-GFP and Bcl-xL KO-mCherry cells (nonclonal) were mixed at a 1:1 ratio 24 hours before implantation and proportions were confirmed by flow cytometry. A mixture containing 8×10^6 cells in DMEM was inoculated into the flanks of NOD.SCID mice (males and females) and harvested when tumors reached 7–9 mm in diameter. TMR-dextran 70 kDa was injected retro-orbitally 30 minutes prior to sacrifice. For each mouse, two sections representing different regions of the tumor were analyzed for relative thresholded area and spatial distribution (relative to dextran signal) of EV-GFP and Bcl-xL KO-mCherry cells.

Intratumoral injections

PANC1-GFP xenografts were established by injection of 8×10^6 cells in DMEM into the flanks of male or female NOD.SCID mice. Tumors were allowed to grow to 7–9 mm in diameter and then injected intratumorally using a 27 g needle with 50 µL with either PBS, A-1155463 (Cayman Chemical, 1.25 mg/mL) in buffer containing 10% DMSO, 40% PEG300, 51% T80, 45% saline, buffer alone gemcitabine (Pfizer, 1 mg/mL) + albumin-conjugated paclitaxel (abraxane, 0.6 mg/mL) at a rate of approximately 50 µL/minute. Twenty-four hours postinjection, Texas red-dextran 70 kDa was injected retro-orbitally 30 minutes prior to sacrifice. Four to 6 sections per mouse (from different regions) were evaluated for apoptosis rates in GFP$^+$ cells.

Long-term drug treatment

MH6620c1 subcutaneous tumors were established by inoculation of 3×10^5 cells in DMEM to the flanks of C57BL/6J male mice and allowed to grow to 6–9 mm. Mice were then randomly assigned to one of four groups receiving the following treatments: 120 mg/kg gemcitabine (Pfizer) + 120 mg/kg nab-paclitaxel (abraxane) twice weekly intraperitoneally, 10 mg/kg of A-1331852 ChemieTek) in buffer containing 10% EtOH, 27.5% PEG400 and 60% Phosal 50G by oral gavage, combined chemotherapy+ A-1331852, A-1331852 buffer alone by gavage + PBS injection. Tumor size was measured by calipers.

Statistical analysis

Comparisons between two groups were performed using Student unpaired t test. One-way ANOVA with Dunnett, Holm–Sidak, corrections for multiple testing was applied as described for each analysis. All statistical analyses were performed with GraphPad Prism 9 (GraphPad). Error bars show SEM unless otherwise indicated, and $P < 0.05$ was considered statistically significant (*, $P < 0.05$; **, $P < 0.01$; ***, $P < 0.001$; and ****, $P < 0.0001$; ns, not significant). For sequencing experiments, DESeq2 (26) was used to generate adjusted P values (FDR). For The Cancer Genome Atlas (TCGA) survival analysis, KM plotter (27) was used to generate log-rank P values.

Data availability statement

The data generated in this study are publicly available in Gene Expression Omnibus (GEO) under the accession number GSE176076 or are available within the article and its Supplementary Data files.

Results

Modeling metabolic heterogeneity in pancreatic cancer

Pancreatic ductal adenocarcinoma (PDAC) is a highly nutrient-depleted and hypoxic tumor type due to its dense stroma and low vascularity (28–31). As a result, most PDAC cancer cells cycle slowly *in vivo* (32–35). The altered metabolic milieu within tumors (36) stands in contrast to standard culture conditions, where PDAC cancer cells have access to supraphysiologic quantities of amino acids, sugars, lipids, oxygen, and growth factors and exhibit a high proliferative index. We therefore hypothesized that the low proliferation rate of cancer cells *in vivo* reflects a reduced availability of blood-borne oxygen and nutrients. To test this, we introduced 70-kDa Texas Red–conjugated dextran into autochthonous pancreatic tumor–bearing KPCY animals (32) by intravenous (i.v.) injection and measured red fluorescence as a surrogate for perfusion (Supplementary Fig. S1A). We then identified regions that were dextran-high ("well perfused") or dextran-low ("poorly perfused"; see Materials and Methods) and compared rates of tumor cell proliferation by measuring 5-ethynyl-2′-deoxyuridine (EdU) incorporation and Ki-67$^+$ staining in YFP$^+$ cancer cells. As expected, cancer cells in well-perfused areas exhibited a significantly higher rate of proliferation (**Fig. 1A** and **B**; Supplementary Fig. S1B). In contrast, rates of apoptosis, as measured by staining for CC3, were not different between well-perfused and poorly perfused regions (**Fig. 1A** and **B**). These results are consistent with the notion that pancreatic tumors are metabolically heterogeneous (37), and that cancer cells in poorly perfused regions acquire a slow-cycling, viable state.

To establish an *in vitro* experimental system that recapitulates the quiescent state associated with nutrient poor, hypoxic conditions *in vivo*, we varied media composition and oxygen concentrations to identify conditions that resulted in a significant reduction in cell proliferation without loss of cell viability (Supplementary Fig. S1C and S1D). Using PANC1 cells, we found that DMEM supplemented with 2.5 mmol/L glucose, 0.5% FBS, and 20% of standard amino acid concentration fulfilled this goal when cells were grown at an oxygen concentration of 1% (**Fig. 1C**), noting that this does not necessarily mimic *in vivo* conditions. Under these "arid" conditions, cells had reduced DNA synthesis (**Fig. 1D**) but no increase in cell death (**Fig. 1E**) as compared with cells grown under standard "fertile" conditions (DMEM with 25 mmol/L glucose, 10% FBS, 100% amino acids, 20% oxygen). Cell labeling with PKH26, a fluorescent dye that is diluted with each round of cell division, indicated a dramatic change in doubling time associated with the transition to arid conditions, increasing nearly 5-fold after 7 days and nearly 18-fold after 21 days (**Fig. 1F**; Supplementary Fig. S1E). Importantly, slow-cycling cancer cells resumed normal proliferation after a return to fertile conditions, indicating that they had not entered an irreversible growth arrested state (**Fig. 1F**). Similar results were obtained with a KPCY-derived mouse cell line, MH6620c1 (Supplementary Fig. S1F–S1H; ref. 17).

Next, we assessed the effect of arid conditions on other metabolic phenotypes. Consistent with prior studies (38–40), nutrient and oxygen deprivation prompted a significant decrease in protein synthesis measured by O-propargyl-Puromycin (OPP) incorporation (**Fig. 1G**) as well as a significant increase in metabolic scavenging pathways, including autophagy and macropinocytosis (**Fig. 1H** and **I**). These changes were associated with a decrease in cell size (Supplementary Fig. S1I). As expected, steady-state metabolomics of cells grown for 7–14 days under arid condition revealed a depletion of TCA cycle intermediates and most acyl-CoAs as well as a reduction in

intracellular amino acid pools (Supplementary Fig. S2A and S2B; Supplementary Table S1). These changes in metabolite levels were associated with approximately 50% reduction in intracellular ATP (**Fig. 1J**). These results indicate that combined nutrient and oxygen deprivation results in a severe depletion of intracellular biofuels and a hypoenergetic state.

Cells grown under arid conditions for 2 days exhibited dramatic changes in gene expression, with 3,196 genes upregulated and 2,687 genes downregulated ($P_{adj} < 0.05$) compared with cells grown under fertile conditions (Supplementary Fig. S3A). Functional annotation by gene-set enrichment analysis (GSEA) revealed the hypoxia–HIF response to be the most highly induced gene set, with related stress responses including glycolysis, autophagy, NFκB, and cell cycle–inhibitory pathways also exhibiting upregulation (Supplementary Fig. S3B). Oxidative phosphorylation (OXPHOS) and pathways associated with proliferation, such as targets of MYC and E2F, dominated the transcriptional profile of genes downregulated under arid conditions (Supplementary Fig. S3C). Components of the TCA cycle and the electron transport chain were also downregulated (Supplementary Fig. S3D), as were genes involved in nucleic acid and protein synthesis (Supplementary Fig. S3E). These results indicate that adaptation to arid conditions is associated with widespread transcriptional reprogramming, resulting in the induction of glycolytic and autophagic pathways and repression of TCA cycle and biosynthetic pathways. To confirm that the gene expression changes associated with arid adaptation *in vitro* is consistent with regulatory events occurring *in vivo*, we stained tumors for three proteins whose mRNA levels decreased under arid conditions (Supplementary Fig. S4A). All three exhibited the expected expression pattern *in vivo*—high in perfusion-proximal regions and low in perfusion-distal regions (Supplementary Fig. S4B)—suggesting that arid conditions model at least some of the adaptations experienced by cells in poorly perfused regions of the tumor.

Finally, to determine whether the slow-cycling state impacts sensitivity to chemotherapy, we examined the dose response of PANC1 cells to gemcitabine. Under fertile conditions, cells were sensitive at an IC_{50} of 16.63 μmol/L, similar to previous findings (**Fig. 1K**; ref. 41). In contrast, cells grown under arid conditions were fully resistant to gemcitabine, even at a dose of 1 mmol/L (**Fig. 1K**) as expected on the basis of gemcitabine's activity as an inhibitor of DNA synthesis. These results suggest that metabolically deprived slow-cycling tumor cells represent a chemoresistant subpopulation, a result we later confirmed *in vivo* (see below).

CRISPR screening identifies genes that are either essential for, or detrimental to, adaptation to arid conditions

We hypothesized that cellular adaptations to metabolic deprivation might be associated with selective (and exploitable) gene dependencies. To identify such dependencies, we performed a genome-wide CRISPR screen utilizing Cas9-expressing PANC1 cells and the Brunello sgRNA library, which targets more than 19,000 genes (18). Cancer cells were first allowed to grow in fertile medium to allow short- or long-term depletion of sgRNAs targeting genes required for cell viability under standard culture conditions. At day 9 and day 32 after transduction (denoted as early and late fertile references points), transduced cells were subcultured and propagated under arid conditions or fertile conditions for an additional 21 days. Genomic DNA was extracted 3 days after transduction to account for library representation (T_0), at early and late reference points (d9 fertile, d32 fertile), and at both 21-day endpoints (d30 arid, d30 fertile; d53 arid, and d53 fertile; **Fig. 2A**).
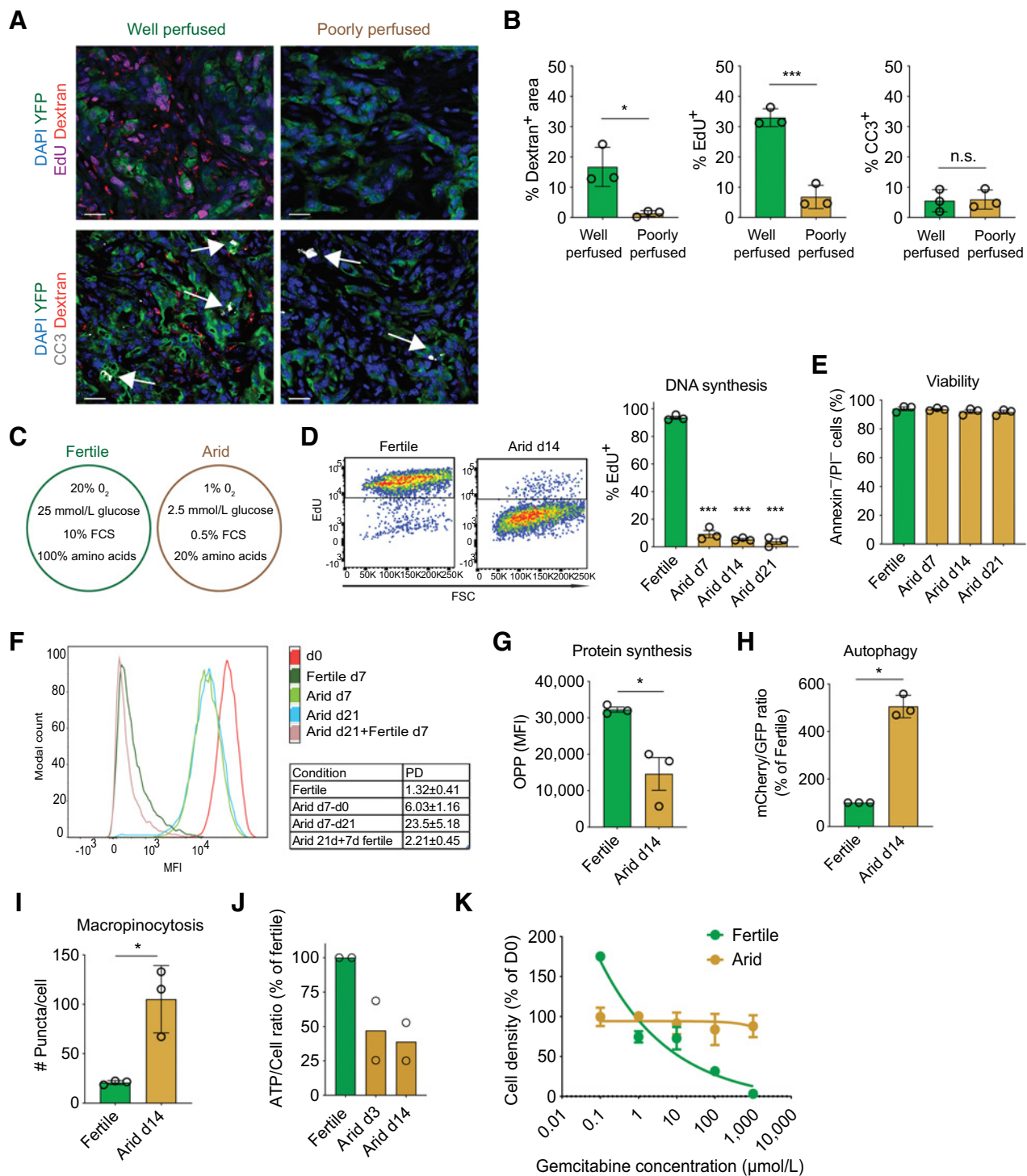
Figure 1.
An *in vitro* system recapitulates phenotypes associated with hypoperfused regions of pancreatic tumors. **A,** Representative confocal images indicating the frequency of proliferating (EdU+, magenta) and apoptotic (CC3+, gray) cells in well perfused and poorly perfused regions in KPCY tumors (Texas Red dextran; red) detected by coimmunofluorescence. Arrows, CC3+ apoptotic tumor cells. Scale bar, 25 μm. **B,** Dextran staining was used to distinguish well perfused and poorly perfused regions of the KPCY mice in **A** (see Materials and Methods). Quantification of the fraction of GFP+ tumor cells that were EdU+ or CC3+ in either region is shown (data pooled from *n* = 3 tumors, 3 sections per tumor and 5 regions per section). **C,** "Fertile" (green) and "Arid" (orange) culture conditions employed *in vitro*. **D,** Representative flow cytometry dot plot and quantification of EdU+ PANC1 cells following a 24-hour pulse under fertile conditions or after 7, 14, or 21 days of arid conditions (data pooled from *n* = 3 experiments, two to three replicates per experiment). **E,** Flow cytometry–based Annexin/PI measurements of PANC1 cells maintained under fertile and arid conditions (data pooled from *n* = 3 experiments, two to three replicates per experiment). (*Continued on the following page.*)

We first sought to determine which genes and pathways are essential under fertile conditions but not arid conditions. As expected, such genes were predominantly associated with cell growth programs including cell-cycle progression and biosynthesis (Supplementary Fig. S5A; Supplementary Tables S2 and S3). For example, sgRNAs targeting genes regulating cell proliferation (e.g., MYC, DBF4, and CCNB1) or translation (e.g., EIF4A1, RPL12, and RPL5) were depleted prior to the early reference point and further depleted following an additional 21 days of culture under fertile conditions (**Fig. 2B**, compare d9 fertile to d30 fertile). In contrast, there was little selection against these genes following transfer to arid conditions (**Fig. 2B**, compare d9 fertile to d30 arid). These results confirm that this screening approach identifies differential genetic dependencies of cells grown under fertile versus arid conditions.

We next performed the reciprocal analysis to identify genes and pathways necessary under arid conditions but not fertile conditions. This was achieved by identifying sgRNAs that are depleted in both early (d30) and late (d53) arid conditions but not under any fertile conditions. Unfiltered functional annotation of genes targeted by these sgRNAs revealed an association with components of the electron transport chain and the TCA cycle (**Fig. 2C**). For example, sgRNAs targeting components of mitochondrial complex I (e.g., NDUFB10, NDUFC1, and UQCC1) or the TCA cycle (e.g., MDH2, MPC1, and SUCLG1) were among the top hits depleted under arid conditions, whereas there was little selection under fertile conditions (**Fig. 2D**, compare d32 reference to d53 arid vs. fertile; Supplementary Fig. S4C and S4D; Supplementary Tables S2 and S3). As arid conditions induce a slow-cycling state, the observed dependencies likely reflect a requirement for cell survival rather than a requirement for cell growth and proliferation.

To confirm the vulnerabilities identified in our CRISPR screen, we measured the sensitivity of cells grown under arid or fertile conditions to a panel of small-molecule inhibitors. In agreement with our observations from gemcitabine treatment (**Fig. 1F**), inhibitors targeting the cell-cycle regulator DBF4 (PHA767491; ref. 42) or the translation initiation factor EIF4A1 (Silvestrol; ref. 43) caused a dose-dependent growth arrest of PANC1 cells under fertile conditions but had little effect under arid conditions (Supplementary Fig. S5B). Conversely, cells grown under arid conditions were highly sensitive to inhibitors targeting the TCA cycle such as devimistat (CPI-613; ref. 44) or the mitochondrial pyruvate carrier MPC1 such as 2-cyano-3-(1-phenyl-1H-indol-3-yl)-2-propenoic acid (UK-5099; ref. 45), whereas these drugs had no effect on the survival of cells grown under fertile conditions, even at high micromolar concentrations (**Fig. 2E**). Similar drug response profiles were observed in AsPC-1 and HPAC cells (Supplementary Fig. S5C and S5D).

Because arid conditions prompted a reduction in DNA and protein synthesis (**Fig. 1D** and **G**; Supplementary Fig. S3), we hypothesized that anabolic processes might be detrimental to cell survival during nutrient and oxygen deprivation. To this end, we reexamined our CRISPR data for sgRNAs that were enriched, rather than depleted, under arid but not fertile conditions. Functional annotation indicated an enrichment for target genes involved in cell-cycle progression and biosynthesis as well as targets of the PRC2 complex (**Fig. 2F**). Conversely, sgRNA targeting several genes that suppress biosynthesis were depleted under arid conditions (Supplementary Tables S2 and S3) including tuberous sclerosis 2 (TSC2). TSC2 is a negative regulator of mTOR, a master regulator of cell growth (46), and thus its loss would be expected to trigger inappropriate growth and proliferation under metabolically adverse conditions. To test this hypothesis, we generated PANC1 cell lines lacking TSC2 and confirmed that this resulted in an acute increase in DNA and protein synthesis (**Fig. 2G** and **H**) and mTOR activity as measured by S6 phosphorylation (**Fig. 2I**). We then performed a competition experiment in which we mixed wild-type (WT) cells (GFP$^+$) with TSC2-deficient cells (mCherry$^+$) at a 1:1 ratio and cultured them under fertile or arid conditions for 7, 14, or 21 days. As shown in **Fig. 2J**, TSC2 wild-type cells out-competed TSC2-deficient cells under arid conditions, while there was minimal difference under fertile conditions. This decrease in TSC2-deficient cell fitness was attributable to a loss of viability under arid, but not fertile conditions (Supplementary Fig. S5E and S5F). Thus, loss of the TSC2 tumor suppressor leads to a paradoxical reduction in the fitness of metabolically deprived cells, in line with its protective role against hypoxia-induced energy stress (46).

Taken together, these results indicate that certain pathways sustain cell survival under arid conditions while other pathways hinder survival. The first category consists of genes involved in the TCA cycle and OXPHOS, which may reflect a heightened dependency on ATP production or other metabolites generated by these pathways. The second category consists of genes involved in negative control of growth and proliferation, suggesting that enforced biosynthesis in the absence of adequate nutrient and oxygen availability is detrimental for cell survival. Hence, the reduction in anabolic activity following nutrient and oxygen deprivation is not merely a consequence of changing metabolic conditions but instead is an essential adaptation.

Arid conditions create a selective and nonredundant dependency on Bcl-xL

Inhibitors of the TCA cycle and OXPHOS, including the TCA cycle inhibitor CPI-613, have demonstrated efficacy in PDAC preclinical models (47–49) but limited success in PDAC clinical trials (https://www.healio.com/news/hematology-oncology/20211028/devimistat-regimen-fails-to-extend-os-in-metastatic-pancreatic-cancer; ref. 50). Therefore, we reexamined our CRISPR data to identify other tractable vulnerabilities specific to metabolically deprived slow-cycling cells. Among genes exclusively depleted under both early and late arid conditions, but not under fertile conditions, the BCL2 family member *Bcl2l1*, encoding Bcl-xL, stood out as one of the most

---

(*Continued.*) **F,** Representative histograms and quantification of proliferation kinetics based on PKH26 dilution. The table shows population doubling (PD) times calculated for the various conditions. Data in table represents the mean ± SEM of $n = 3$ experiments, three replicates per experiment. **G,** Measurement of protein synthesis in PANC1 tumor cells pulsed with OPP for 1 hour (data pooled from $n = 3$ experiments, two replicates per experiment). **H,** Measurement of autophagy by quantification of mCherry$^+$/GFP$^+$ ratios of PANC1 cells expressing the autophagy reporter GFP-mCherry-LC3B (data pooled from $n = 3$ experiments, two replicates per experiment). **I,** Measurement of macropinocytosis by quantification of intracellular puncta following exposure of PANC1 cells to TMR-dextran (red) for 30 minutes (data pooled from $n = 3$ experiments, two replicates per experiment). **J,** Measurement of intracellular ATP levels (per cell) in PANC1 cells determined by CellTiter-Glo luminescence, normalized to microscopy-based nuclear count (data pooled from $n = 2$ experiments, four replicates per experiment). **K,** Chemosensitivity analysis of PANC1 cells treated with the indicated doses of gemcitabine (5 days). Viability was determined by comparing nuclear counts at treatment endpoint compared to onset (data pooled from $n = 2$ experiments, two replicates per experiment). In **B** and **G–I**, statistical differences were calculated using unpaired *t* test and in **D**, statistical differences were calculated using one-way ANOVA and Dunnett test (comparing to fertile). $P < 0.05$ was considered statistically significant. *, $P < 0.05$; ***, $P < 0.001$; n.s., not significant.
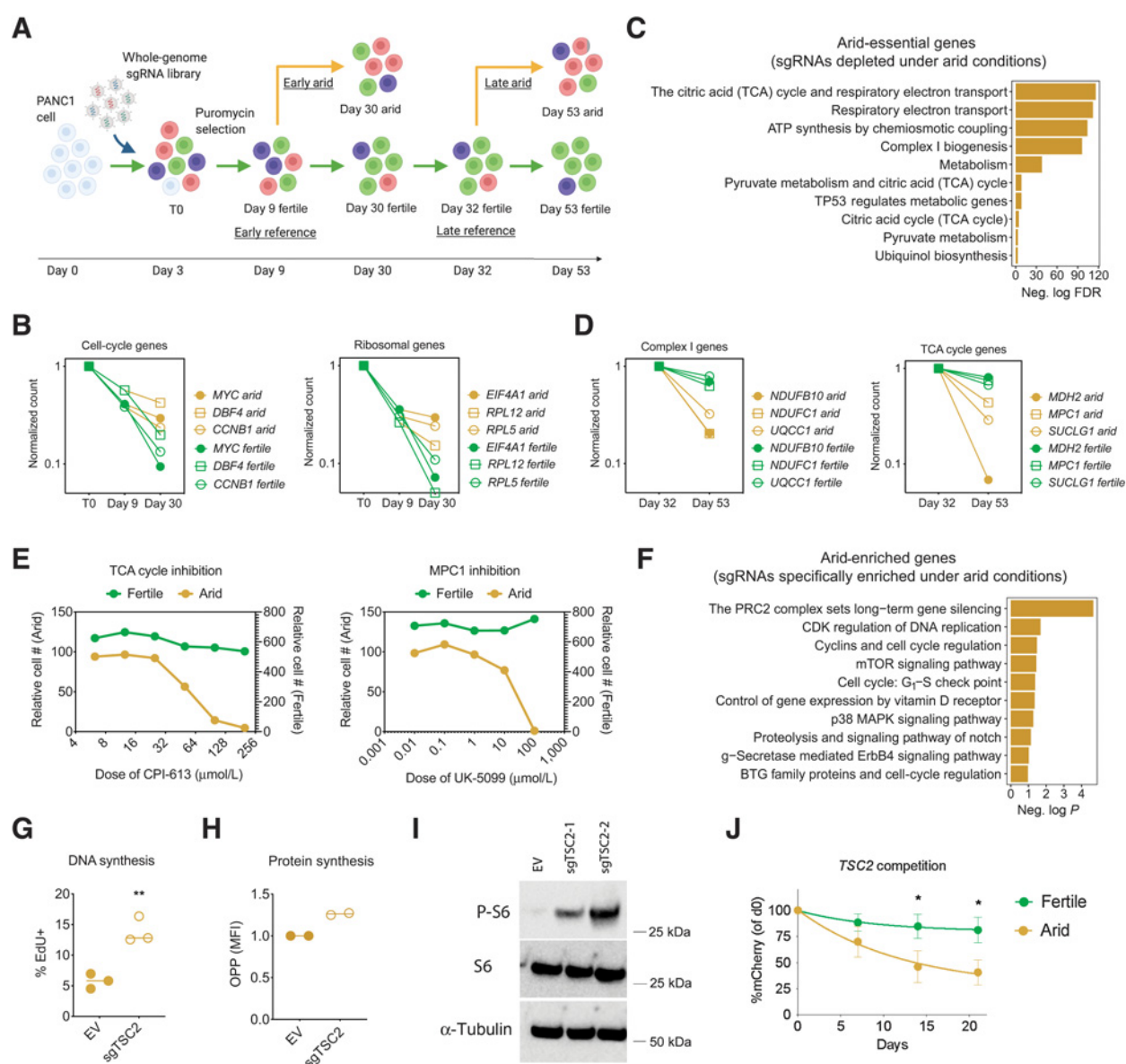
Figure 2.
Genome-wide CRISPR screening reveals contrasting dependencies for cells under fertile vs. arid conditions. **A,** Schematic showing the screening strategy (see text for details). **B,** Normalized abundance counts for sgRNAs reflecting essential genes under fertile conditions (depleted in fertile d9 vs. T0 and d30 fertile vs. d9 fertile but not d30 arid vs. d9 fertile). **C,** Unfiltered functional annotation by Reactome ($P < 0.05$) of sgRNAs depleted in both early (d30 arid vs. d9 fertile) and late exposures (d53 arid vs. d32 fertile) to arid conditions but not fertile conditions (d9 fertile vs. T0, d30 fertile vs. d9 fertile, or d53 fertile vs. d32 fertile). **D,** Normalized abundance counts for sgRNAs reflecting essential genes under arid conditions (depleted in d53 arid but not d53 fertile compared with d32 fertile). **E,** Drug–response curves for CPI-613 and UK-5099 targeting the TCA cycle and MPC1, respectively. Normalized cell counts for cells grown under arid conditions (left vertical axes) versus fertile conditions (right vertical axes) are different given the slow cycling nature of the former and the rapidly proliferating status of the latter (datapoints are the means of $n = 2$ experiments). **F,** Unfiltered functional annotation by Biocarta (FC>1.33, $P < 0.05$) of sgRNAs enriched under arid conditions (d30 arid vs. d9 fertile but not d30 fertile vs. d9 fertile). **G** and **H,** Quantification of DNA synthesis by EdU incorporation (**G**) and protein synthesis by OPP incorporation (**H**) after 7 days of arid conditions, comparing sgTSC2 to control (EV). EdU data pooled from $n = 3$ experiments, two replicates; OPP data pooled from $n = 2$ experiments, two replicates each. **I,** Immunoblot of total S6 and phospho-S6 levels in control PANC1 cells (EV) or cells lacking TSC2 (sgTSC2) following 3 days under arid conditions. **J,** Results of competition between EV-GFP cells and mcherry-sgTSC2 cells, with samples collected at the indicated time points (data pooled from $n = 3$ experiments, two replicates per experiment). In **G**, statistical differences were calculated using t test. In **J**, statistical differences were calculated using multiple t tests. $P < 0.05$ was considered statistically significant. *, $P < 0.05$; **, $P < 0.01$.

strongly selected genes (**Fig. 3A**) and its expression increased under arid conditions (**Fig. 3B**). Bcl-xL is best known for its ability to inhibit apoptosis (51, 52), but it also regulates mitochondrial function (52) and cell-cycle progression (53, 54). Given that these three

cellular activities are features of the metabolic adaptation in our experimental system, we hypothesized that arid conditions create a selective dependency on Bcl-xL that is not shared by pancreatic cancer cells under fertile conditions. No other canonical BCL2 family
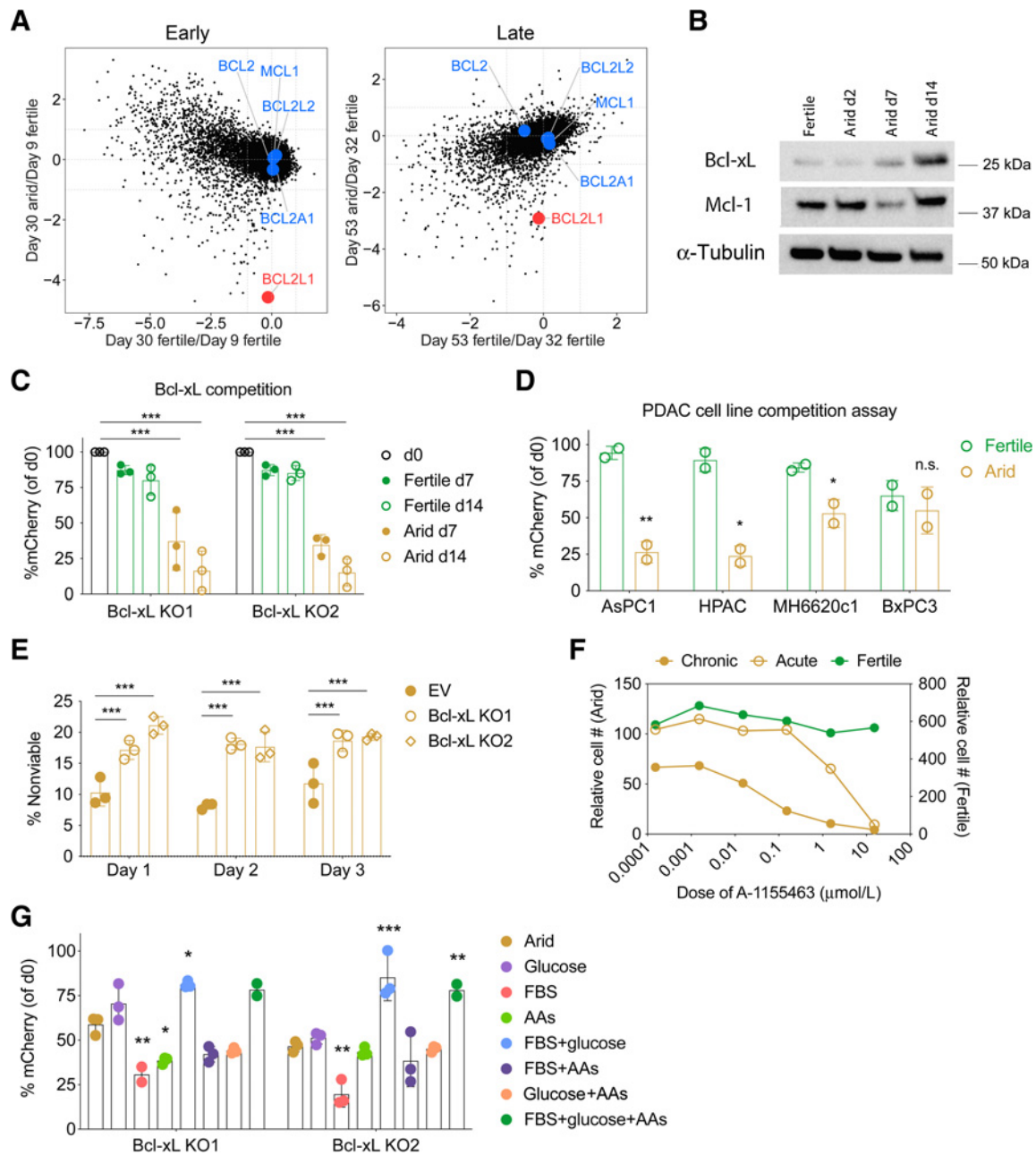
Figure 3.
Bcl-xL is essential and nonredundant under arid conditions. **A,** Dot plot showing log-fold change in sgRNA abundance (each dot represents the pool of sgRNAs targeting a single gene) of cells maintained in fertile conditions (x-axis) or switched to arid conditions (y-axis) at early (left) and late (right) time points of the CRISPR screen. The adjusted P values for Bcl-xL (BCL2L1, red) are 1.81×10^{-6} and 1.17×10^{-5}, respectively. Other Bcl2 family members did not show a significant change and are highlighted (blue). **B,** Western blots showing the expression of Bcl-xL and Mcl-1 under fertile and arid conditions. **C,** Results of competition between EV-GFP and Bcl-xL KO-mCherry PANC1 clones grown under fertile or arid conditions for the indicated times (data pooled from $n = 3$ experiments, 2–3 replicates per experiment). **D,** Results of competition in a panel of human and mouse cell lines lacking Bcl-xL under fertile and arid conditions (data pooled from $n = 2$ experiments, 1–2 replicates per experiment). Cells were sampled at different time points according to their survival capacity under arid conditions. AsPC-1 (3d), HPAC (7d), BxPC3 (7d), and MH6620c1 (14d). **E,** Quantification of nonviable cells in EV and Bcl-xL KO PANC1 clones following transfer to arid conditions, determined by flow cytometry for Annexin V and DAPI (data pooled from $n = 3$ experiments, two to three replicates per experiment). **F,** Dose response of PANC1 cells treated with Bcl-xL inhibitor A-1155463 for 4 days. Cells were grown in either fertile conditions throughout ("Fertile"), transferred to arid conditions at the onset of treatment ("Acute") or preacclimated to arid conditions for 14 days before treatment began ("Chronic"). Cell numbers are plotted relative to cell number at the beginning of treatment and are the means of $n = 2$ experiments. **G,** Results of competition between EV and Bcl-xL KO-mCherry PANC1 clones following addback of various nutrients in the presence of 1% O_2 (data pooled from $n = 3$ experiments, two replicates per experiment). In **C, E,** and **G,** statistical differences were calculated using one-way ANOVA and Dunnett test [comparing with d0 (**C**), EV (**E**), and baseline arid (**G**)]. In **D,** statistical differences were calculated using t tests. For **G,** significance is indicated relative to baseline (arid) conditions. $P < 0.05$ was considered statistically significant. *, $P < 0.05$; **, $P < 0.01$; ***, $P < 0.001$; n.s., not significant.

members were enriched or depleted under either fertile or arid conditions (**Fig. 3A**), suggesting that Bcl-xL may have a unique function in slow-cycling metabolically deprived cancer cells.

We first confirmed the dependency for Bcl-xL by knocking out the *BCL2L1* gene with two independent sgRNAs (Supplementary Fig. S6A). In line with our CRISPR screen results, Bcl-xL–deficient cells exhibited reduced fitness in a competition assay under arid but not fertile conditions (**Fig. 3C**) and were eliminated even if cells were already adapted to arid conditions (Supplementary Fig. S6B). This requirement for Bcl-xL was validated in two additional human PDAC cell lines (AsPC-1 and HPAC), a murine PDAC cell line (MH6620c1), and 5 other non-PDAC cancer cell lines (**Fig. 3D**; Supplementary Fig. S6C and S6D). Interestingly, BxPC3 cells, which lack a KRAS mutation, did not show differential dependence. Cell viability was high and comparable between empty vector (EV) and Bcl-xL–deficient cells under fertile conditions (Supplementary Fig. S6E). In contrast, Bcl-xL–deficient cells exhibited decreased viability within 1 day of culture under arid conditions (**Fig. 3E**). Therefore, Bcl-xL protects pancreatic cancer cells from cell death following nutrient and oxygen deprivation but is dispensable under nutrient replete conditions.

To further confirm this Bcl-xL dependency, we employed a potent and highly selective Bcl-xL inhibitor, A-1155463, which is based on the 2-(fluorophenoxy)propyl)thiazole-4-carboxylic acid structure (55). Exposure of either PANC1, MH6620c1, AsPC-1, or HPAC cells to A-1155463 *in vitro* resulted in a significant dose-dependent loss of viability under arid conditions, whereas the drug had no effect on cells under fertile conditions, even at doses over 10 μmol/L (**Fig. 3F**; Supplementary Fig. S6F–S6H). A1155463-mediated cell death was inhibited by the pan-caspase inhibitor Z-VAD-FMK (Supplementary Fig. S6I), indicating that apoptotic cell death contributed at least partially to the reduced fitness of Bcl-xL–deficient cells grown under arid conditions.

Because the arid medium composition was determined empirically, we sought to determine whether the dependency on Bcl-xL extended to physiologically defined metabolic conditions. To this end, we exploited tumor interstitial fluid medium (TIFM) – media defined by direct measurement of metabolite concentrations in the interstitial space of murine pancreatic tumors (36). Consistent with our results using arid medium, PANC1 cells grown in TIFM medium (1% O_2) were also dependent on Bcl-xL for survival (Supplementary Fig. S7A and S7B). Moreover, cells grown in arid or TIFM medium showed similar sensitivity to the Bcl-xL inhibitor A-1155463 (Supplementary Fig. S7C). Hence, Bcl-xL function is required for cell survival under diverse conditions of metabolic deprivation.

Bcl-xL exerts protective effects under a variety of stress conditions (52). To determine what triggers Bcl-xL dependency under arid conditions, we conducted "add-back" experiments in which we reintroduced various nutrients—either alone or in combination and under hypoxic or normoxic conditions—and then assessed the proportions of two Bcl-xL–deficient tumor cell clones in competition with EV cells. No single nutrient, or normoxia, was able to rescue either Bcl-xL–deficient clone under hypoxic conditions (**Fig. 3G**; Supplementary Fig. S7D). Paradoxically, reintroducing 10% FBS exacerbated depletion of Bcl-xL–deficient cells, while coaddition of FBS and glucose together rescued the phenotype (**Fig. 3G**), suggesting that Bcl-xL may be particularly important under conditions where "biosynthetic pressure" is high, but carbon fuel is low (see Supplementary Fig. S1C). Taken together, these results suggest that metabolic deprivation creates a selective and nonredundant dependency on Bcl-xL.

Bcl-xL promotes the survival of cancer cells in poorly perfused tumor regions

To test whether Bcl-xL is essential for pancreatic cancer cells *in vivo*, we inoculated empty vector (GFP+) or Bcl-xL–deficient (mCherry+) PANC1 cells into the flanks of NOD.SCID mice. Consistent with their reduced viability under arid conditions *in vitro* (**Fig. 3E**), Bcl-xL–deficient cells gave rise to a decreased tumor burden (**Fig. 4A** and **B**; Supplementary Fig. S8) that was associated with a 4–5-fold increase in apoptosis (**Fig. 4C**). Next, we performed a competition experiment in which we subcutaneously implanted control EV-GFP and Bcl-xL–deficient-mCherry tumor cells at a 1:1 ratio, injected TMR-dextran (IV) prior to sacrifice, and examined the resulting tumors. In line with our *in vitro* results, Bcl-xL–deficient tumor cells were consistently depleted but not eradicated in the mixed tumors (**Fig. 4D** and **E**). Analysis of spatial distributions revealed that Bcl-xL–deficient cells were less abundant as the distance from perfused blood vessels increased (**Fig. 4F**), indicating a selective requirement for Bcl-xL in poorly perfused regions.

Next, we sought to determine whether A-1155463 results in a similar perfusion-dependent cell lethality *in vivo*. PANC1-GFP xenografts were allowed to grow to 6–9 mm and then treated with an intratumoral injection of A-1155463 or vehicle for 24 hours, followed by an injection of TMR-dextran prior to sacrifice. Tumors were then sectioned and stained with antibodies against CC3 to quantify apoptosis as a function of distance from perfused blood vessels. GFP+ tumor cells within 200 μm of perfused blood vessels exhibited similar rates of CC3+ staining between A-1155463 and vehicle-treated groups (**Fig. 4G**). In contrast, GFP+ tumor cells >400 μm from perfused blood vessels exhibited a 2–4-fold increase in CC3+ staining in the A-1155463 treatment group (**Fig. 4G**), indicating that sensitivity to Bcl-xL inhibition is positively correlated with distance from perfused blood vessels. We then treated a separate cohort of mice with a combination of gemcitabine and nab-paclitaxel (Gem/nP), which is standard-of-care chemotherapy for PDAC (56), or vehicle control. In contrast to our findings with A-1155463, sensitivity to Gem/nP was limited to GFP+ cells located within 200 μm of perfused blood vessels (**Fig. 4H**). These results complement our *in vitro* studies and suggest that cancer cells residing in well-perfused tumor compartments are more sensitive to cytotoxic chemotherapy while cancer cells residing in poorly perfused tumor compartments are more sensitive to Bcl-xL inhibition.

These findings raised the possibility that simultaneous targeting of proliferating and slow-cycling tumor cells might provide a more potent antitumor effect than either therapy alone. To this end, we established subcutaneous tumors (6–9 mm in diameter) using the murine PDAC clone MH6620c1 and treated tumor-bearing mice with either (i) vehicle, (ii) A-1331852 (an orally available form of A-1155463; ref. 57), (iii) Gem/nP, or (iv) the combination of A-1331852 and Gem/nP (**Fig. 4I**). While either regimen alone had modest effects on tumor volume, the combination of A-1331852 and Gem/nP led to a clear inhibition of tumor growth, including several tumor regressions (**Fig. 4I**). These results provide proof of concept that an approach that targets both the rapid- and slow-cycling compartments of a tumor may provide synergistic therapeutic benefit.

Bcl-xL expression is restricted to slow-cycling cancer cells in human PDAC

We next examined the expression of Bcl-xL (*BCL2L1*) in human PDAC. An analysis of the TCGA dataset revealed *BCL2L1* to be expressed in pancreatic tumors (PAAD) at a higher level compared with most other tumor types (**Fig. 5A**). *BCL2L1* transcripts were significantly more abundant in tumors compared with adjacent
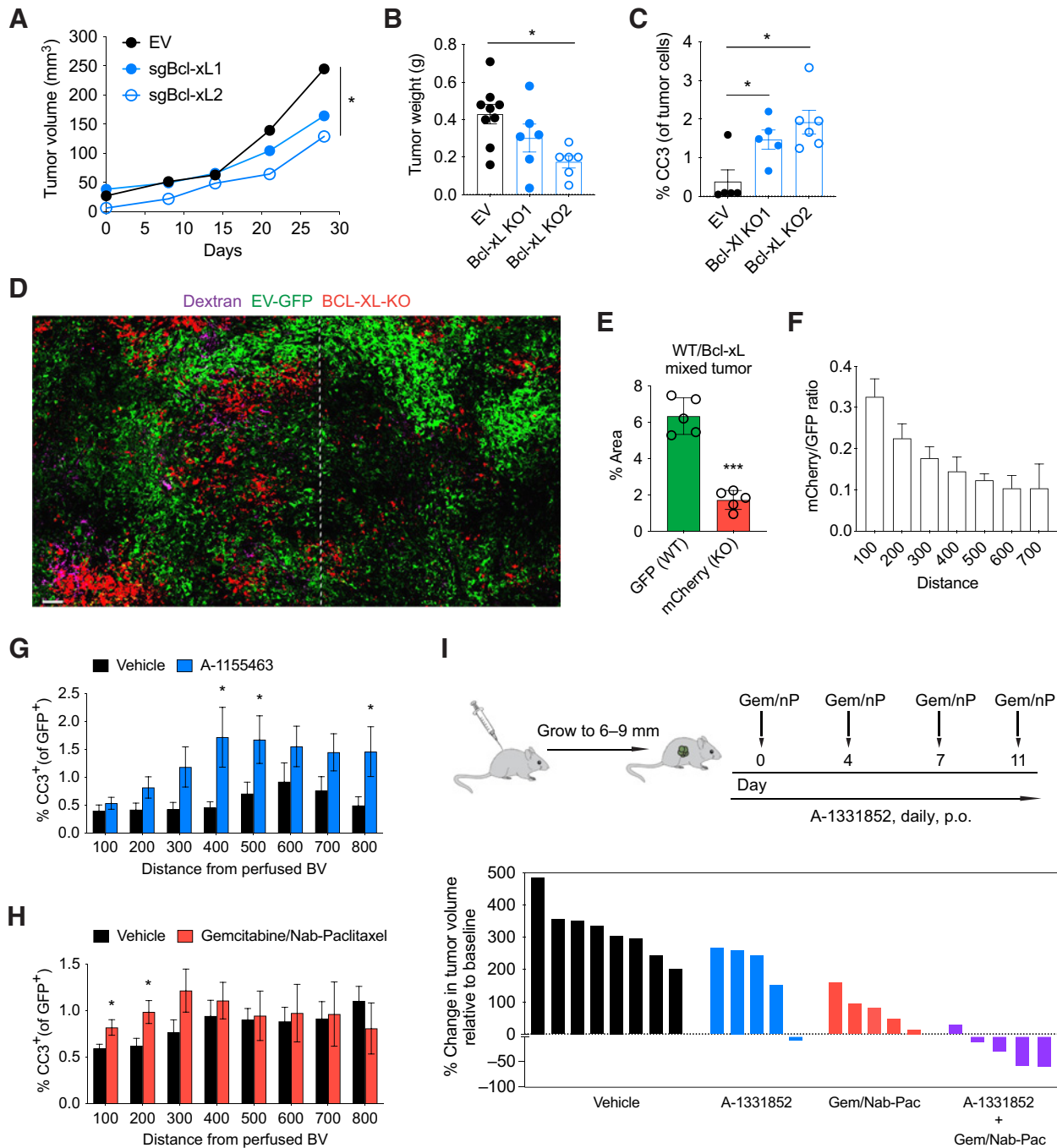
Figure 4.
Bcl-xL is necessary for survival of quiescent PDAC cells *in vivo*. **A,** Measurement of median tumor volumes comparing subcutaneously implanted EV and Bcl-xL KO tumor clones ($n = 8$ EV; $n = 6$ Bcl-xL KO1; $n = 6$ Bcl-xL KO2). **B** and **C,** Measurements of tumor weight (**B**) and apoptotic rate (**C**) in tumors shown in **A**. **D,** Representative confocal image and image-based quantification of EV (green) and Bcl-xL KO (red) mixed tumors. Dashed line approximates well perfused (left) and poorly perfused (right) regions for illustration purposes. Scale bar, 100 μm. **E,** Measurement of the area occupied by Bcl-xL KO-mCherry cancer cells and EV-GFP tumor cells in mixed tumors ($n = 5$). **F,** Ratio between EV-GFP and Bcl-xL KO-mCherry cells as a function of distance from dextran-positive perfused regions in mixed tumors ($n = 5$). **G,** Quantification of the spatial distribution of cleaved caspase-3+ cancer cells in PANC1-GFP xenografts injected intratumorally with A-1155463 or vehicle ($n = 5$). **H,** Quantification of the spatial distribution of cleaved caspase-3+ cancer cells in PANC1-GFP xenografts injected with gemcitabine/nab-paclitaxel or PBS ($n = 5$). **I,** Top, schematic of the experimental strategy for combining gemcitabine and nab-paclitaxel (Gem/nP) with the Bcl-xL inhibitor A-1331852. Bottom, waterfall plots showing final change in the volume of MH6620c1 tumors grown in immunocompetent C57BL/6 hosts following 14 days of treatment. In **A,** statistical differences were calculated using repeated measures one-way ANOVA and Dunnett test (compared with EV). In **B** and **C,** statistical differences were calculated using one-way ANOVA and Dunnett test (comparing with EV) and in **E, G,** and **H,** statistical differences were calculated using *t* tests. $P < 0.05$ was considered statistically significant. *, $P < 0.05$; ***, $P < 0.001$.
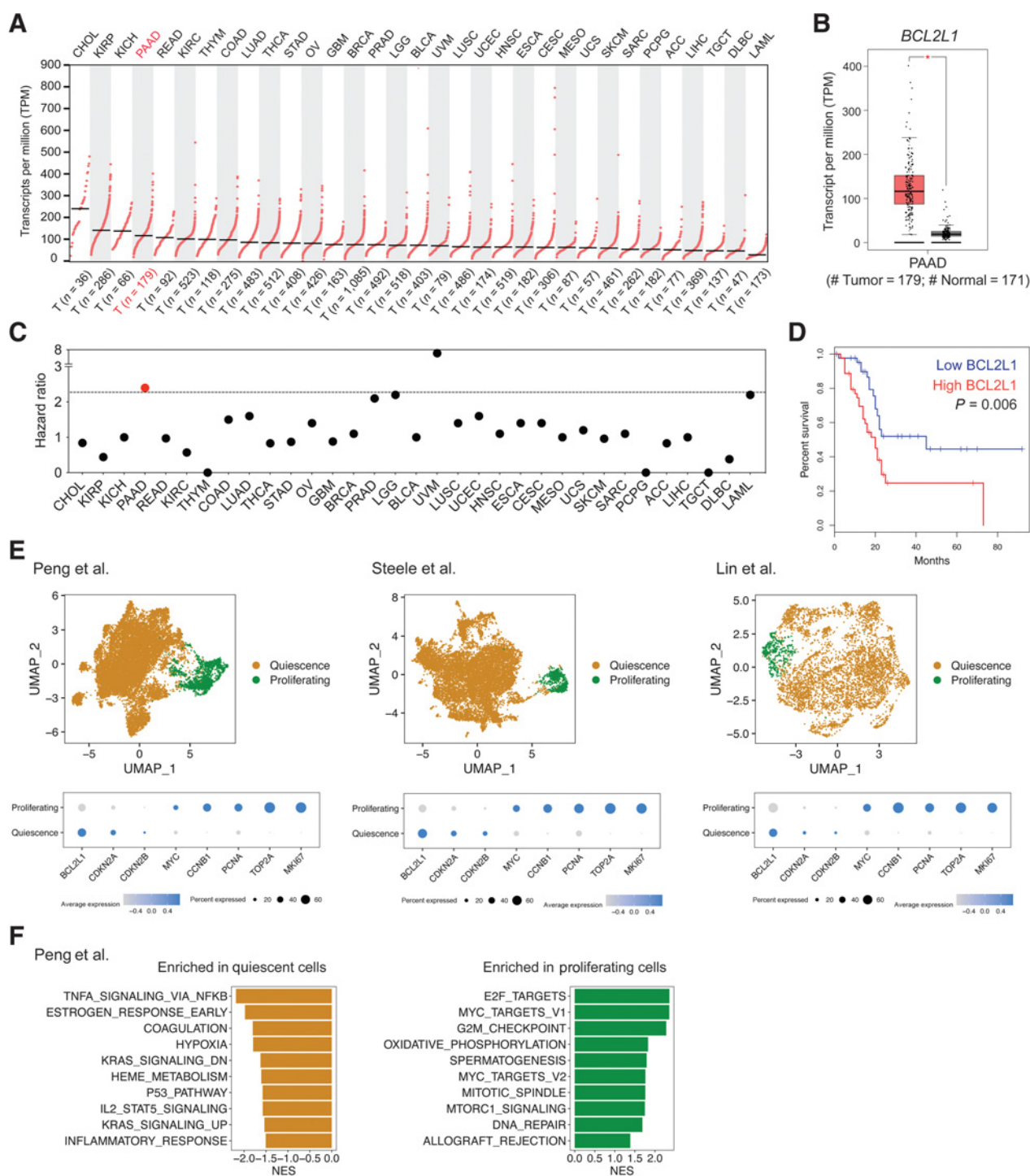
Figure 5.
Quiescent cells in human PDAC exhibit signatures of nutrient and oxygen deprivation. **A,** Relative abundance of BCL2L1 mRNA across tumor types from TCGA data. **B,** Relative abundance of BCL2L1 mRNA comparing PDAC and normal pancreas tissue (TCGA). **C,** Correlation (HR) between BCL2L1 mRNA levels and patient survival across TCGA. **D,** Kaplan–Meier plot showing PDAC survival based on the top (red) and bottom (blue) quartiles of BCL2L1 in PDAC (TCGA). **E,** Top, UMAP plots of single-cell RNA sequencing profiles from three independent studies of human PDAC. The proliferative subpopulation of tumor cells is shown in green, and the quiescent subpopulation of tumor cells is shown in orange. Bottom, relative expression of BCL2L1 and cell-cycle markers segregated into proliferative and quiescent subpopulations. Panels represent pooled data pooled from $n = 24$ (Peng et al.; ref. 59), $n = 10$ (Steele et al.; ref. 60), and $n = 16$ (Lin et al.; ref. 61) tumors, respectively. **F,** Functional annotation by GSEA msGDMIB for Hallmark pathways of upregulated and downregulated genes, comparing quiescent cells with proliferating cells in data from Peng et al. (FDR < 0.05; ref. 59).

normal pancreatic tissue (**Fig. 5B**), consistent with the hypovascular and hypoxic nature of most pancreatic tumors (28, 58). Moreover, *BCL2L1* expression was highly correlated with the overall survival of patients with PDAC compared to patients with other types of cancer (**Fig. 5C** and **D**), a prognostic correlation shared by its closest relative (*BCL2L2*) but no other BCL2 family members (Supplementary Fig. S9A).

To determine whether the expression of *BCL2L1* is linked to slow-cycling state in human cancer, we analyzed three published single-cell RNA-seq (scRNA-seq) datasets (59–61) and annotated cancer cells as either proliferating or quiescent (**Fig. 5E**). In agreement with previous observations (32), only a minority of cancer cells exhibited a proliferative gene signature, while most cancer cells exhibited a slow-cycling gene signature characterized by the expression of *CDKN2A* and *CDKN2B* (**Fig. 5E**; Supplementary Fig. S9B). Consistent with our predictions, expression of *BCL2L1* was markedly higher in the slow-cycling population compared with the proliferating population (**Fig. 5E**).

Next, we examined the functional annotations of genes that were differentially expressed between rapidly and slowly cycling cancer cells in human PDAC. This revealed that the gene programs that distinguished these two populations in human PDAC tumors bore a striking similarity to those that were upregulated or downregulated in PANC1 grown in fertile versus arid conditions *in vitro* (**Fig. 5F**; Supplementary Fig. S9C). Most notably, hypoxia, NFκB, and cell cycle–inhibitory pathways were enriched in slow-cycling cells from both human tumors and arid-cultured cells, while OXPHOS and targets of E2F and MYC were enriched in rapidly cycling cancer cells from both human tumors and fertile-cultured cells (**Fig. 5F**; Supplementary Fig. S9C). Taken together, these results suggest that the genes and pathways found to be dysregulated in our *in vitro* experimental system – including Bcl-xL (BCL2L1) – recapitulate the gene expression features that distinguish the rapidly and slowly cycling compartments of human PDAC tumors.

Bcl-xL protects cells from "inappropriate" biosynthesis

We next investigated the mechanism by which Bcl-xL promotes cell survival under arid conditions. We first performed RNA sequencing of Bcl-xL–deficient and EV-GFP cells grown under arid conditions. Pathways involved in cell-cycle regulation, including targets of MYC and E2F, were the most highly enriched programs in Bcl-xL KO cells (**Fig. 6A**; Supplementary Fig. S10A). Immunoblotting and immunostaining of PDAC cells (PANC1, AsPC-1, HPAC, and BxPC-3) revealed that control cells downregulate MYC protein levels, as well as S6 phosphorylation, under arid conditions, an effect that was blunted in the absence of Bcl-xL (**Fig. 6B**; Supplementary Fig. S10B and S10C). These results suggest that Bcl-xL constrains the biosynthetic and pro-proliferative activities that normally accompany metabolic deprivation.

Bcl-xL has been shown to act as a tumor suppressor by restricting the proliferation of cancer cells in certain contexts (53, 54, 62). In line with these antiproliferative properties, Bcl-xL–deficient cells exhibited a 3–4-fold increase in EdU incorporation under arid conditions (**Fig. 6C**), resulting in over 50% of cancer cells staining positively for Ki-67 (**Fig. 6D**). In contrast, Bcl-xL deficiency had no effect on EdU incorporation or Ki-67 positivity under fertile conditions, where proliferation rates were already high (Supplementary Fig. S10D and S10E). Similar results were obtained following Bcl-xL ablation in additional pancreatic cancer cell lines under arid conditions (Supplementary Fig. S10F). Given that Bcl-xL–deficient cells exhibit increased rates of cell death when cultured under arid conditions (**Fig. 3C**), these

results are consistent with Bcl-xL acting to suppress a "lethal proliferation." Bcl-xL–deficient cells cocultured with control (EV-GFP) cells similarly exhibited increased Ki-67 staining (Supplementary Fig. S10G), indicating that Bcl-xL's proliferation-constraining activity is cell autonomous.

To better understand the relationship between cell-cycle progression and cell death in Bcl-xL–deficient cells, we used a PCNA-interacting protein-fluorescent ubiquitination-based cell-cycle indicator (PIP-FUCCI) reporter, which accurately reports cells in different phases of the cell cycle (**Fig. 6E**; ref. 21). Using time-lapse fluorescent microscopy, we followed the fate of over 800 control (EV) cells or Bcl-xL–deficient cells by direct visualization under either fertile or arid conditions. Using this fate-mapping approach, we observed approximately 3–4-fold increase in G_1–S transitions in Bcl-xL–deficient cells compared with control cells (**Fig. 6F**) but no significant differences in transitions through other phases of the cell cycle (Supplementary Fig. S10H; Supplementary Movies S1–S2) or mitosis (**Fig. 6G**). As expected, the fraction of cells transitioning from G_1 phase to S phase (comparing EV and Bcl-xL–deficient cells) did not increase under fertile conditions (Supplementary Fig. S10I; Supplementary Movies S3–S4). This suggests that the increased S-phase entry caused by Bcl-xL loss does not translate into an increase in cellular progeny.

We next examined our time-lapse microscopy data to determine whether certain phases of the cell cycle were associated with increased cell death in the absence of Bcl-xL. Under arid conditions, control (EV) cells exhibited low rates of cell death in the G_1 (2%) and S (0%) phases of the cell cycle, while 8% of control cells died during the G_2–M phase (**Fig. 6H**). In contrast, Bcl-xL-deficiency was associated with increased cell death at all stages of the cell cycle, particularly during S-phase (20%) and G_2–M (19%; **Fig. 6H**). To determine whether the cell death induced by Bcl-xL knockout was related to this increase in proliferation, we treated cells with the CDK4/6 inhibitor abemaciclib, a potent cell-cycle inhibitor (Supplementary Fig. S10J; Supplementary Movie S5). Abemaciclib treatment rescued cell viability in all stages of the cell cycle (**Fig. 6H**), suggesting that cell-cycle transit is responsible for the increased lethality caused by Bcl-xL loss under arid conditions (53, 62).

Finally, we examined whether Bcl-xL deficiency has similar effects on cell proliferation in PDAC tumors *in vivo*. Tumors derived from control (EV) and Bcl-xL–deficient cancer cells were stained for Ki-67 as a function of distance from a TMR-dextran perfused blood vessel. Control tumors exhibited a typical gradient of Ki-67 staining (higher near blood vessels and lower further away; **Fig. 6I**, left). In contrast, Ki-67$^+$ cells were distributed throughout the axis of perfusion in Bcl-xL–deficient tumors (**Fig. 6I**, right; Supplementary Fig. S10K), giving further support to the notion that Bcl-xL represses proliferation in nutrient-deprived regions of tumors.

Biosynthetic pressure is lethal to metabolically deprived PDAC cells

The results from our CRISPR screen and metabolic "add-back" experiments suggested that biosynthesis and/or proliferation are lethal to metabolically deprived cells, which may lack sufficient resources to meet the demands of cell division. To further explore this hypothesis, we extended our add-back studies, focusing on the addition of serum, which reduced fitness, and glucose, which increased fitness (**Fig. 3G**). Consistent with our previous findings, addition of 10% FBS to cells grown under arid conditions prompted an increase in the fraction of EdU$^+$ cells (**Fig. 7A**) and a concomitant increase in cell death that could be rescued with glucose (**Fig. 7B**). These results suggest that auxiliary fuel sources can overcome the lethal proliferation associated with extreme metabolic deprivation.
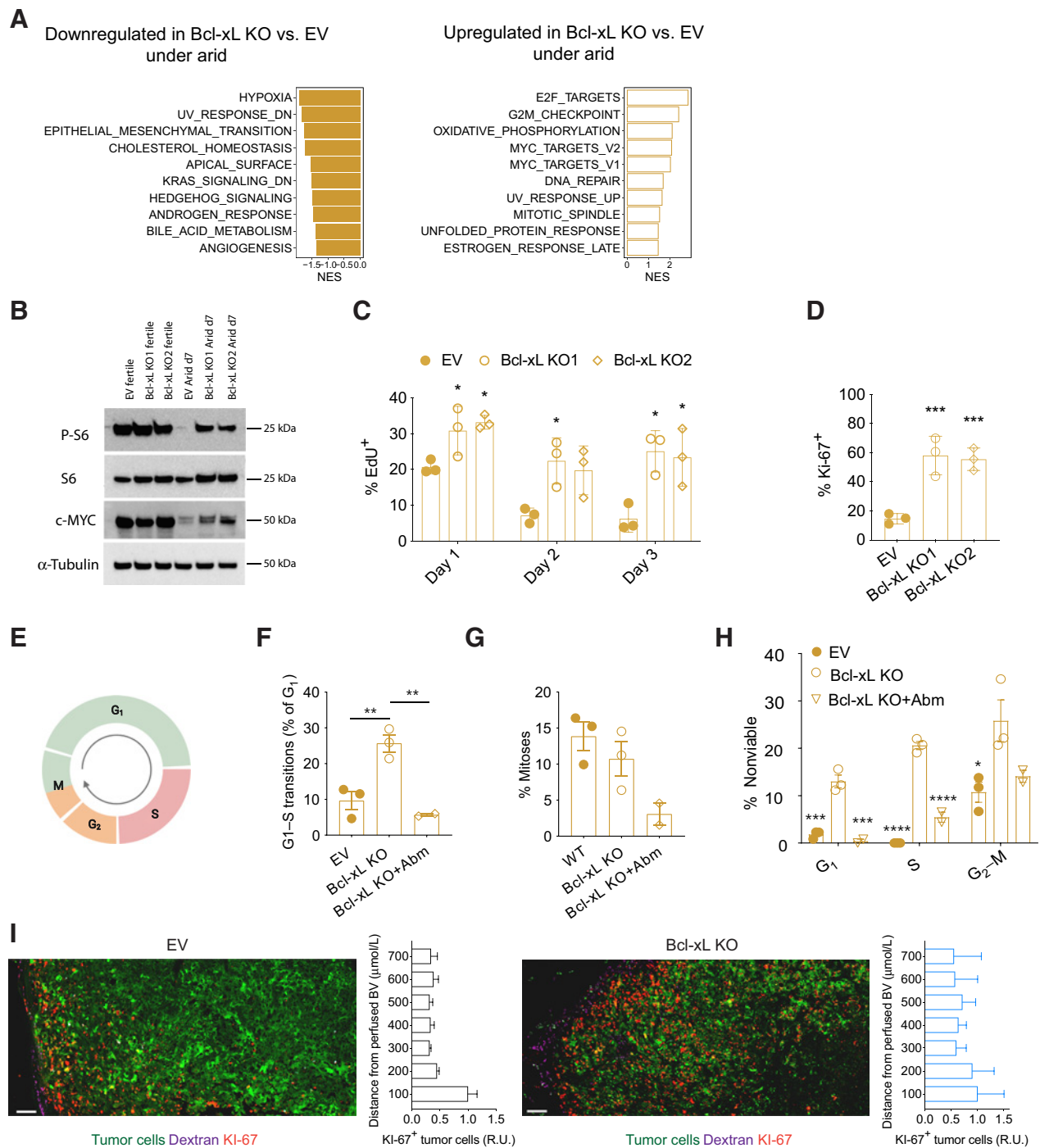
Figure 6.
Bcl-xL protects cells from "inappropriate" biosynthesis. **A,** Functional annotation by GSEA Hallmark pathways of genes upregulated or downregulated in Bcl-xL KO clones compared with EV cells under arid conditions (FDR < 0.05). **B,** Western blots of c-Myc and S6 phosphorylation under fertile and arid conditions in EV and Bcl-xL KO cells. **C,** Flow cytometry–based measurements of EdU^{+} cells in EV and Bcl-xL KO clones (24-hour pulse) during the first 3 days in arid conditions (data pooled from $n = 3$ experiments, two replicates per experiment). **D,** Immunostaining-based quantification of Ki-67^{+} cells in cells cultured at day 7 under arid condition ($n = 3$). **E,** Schematics depicting cell-cycle phase marking by the FUCCI-PIP reporter. **F–H,** Frequency of G_1–S transitions (**F**), frequency of mitotic events (**G**), and frequency of cell death in G_1, S, and G_2 (**H**) comparing control (EV) and Bcl-xL KO (nonclonal) cells tagged with FUCCI-PIP over 48 hours of timelapse microscopy starting at 2 days of arid culture. Results represent the mean of at least three different fields over two to three separate sessions. Abm, Abemaciclib. **I,** Representative confocal images and histogram showing frequency of Ki-67^{+} tumor cells as a function of distance from perfused blood vessels in EV-GFP ($n = 3$) and Bcl-xL KO1-mCherry ($n = 4$) PANC1 cell–derived xenografts. Scale bar, 100 μm. In **C**, **D**, and **F–H**, statistical differences were calculated using one-way ANOVA and Dunnett test (compared with EV). $P < 0.05$ was considered statistically significant. *, $P < 0.05$; **, $P < 0.01$. ***, $P < 0.001$. ****, $P < 0.0001$.
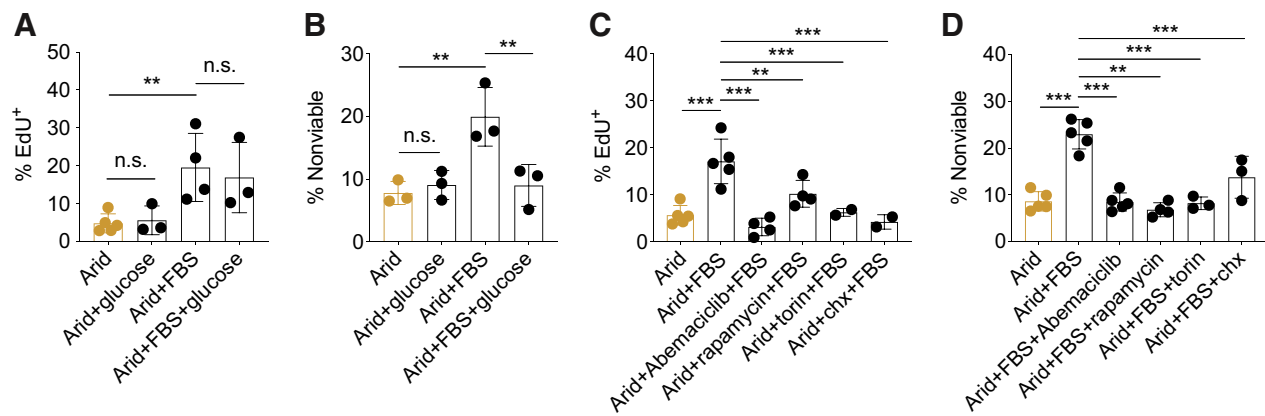
Figure 7.
Biosynthetic pressure under nutrient deprivation is lethal to genetically intact PDAC cells. **A** and **B,** Fraction of EdU$^+$ (**A**) or nonviable (**B**) PANC1 cells cultured under arid conditions for 72 hours with an addback of serum and/or glucose (data pooled from $n = 3–4$ experiments, two to three replicates per experiment). **C** and **D,** Fraction of EdU$^+$ (**C**) or nonviable (**D**) PANC1 cells cultured under arid conditions for 72 hours with an addback of serum in the presence or absence of the indicated biosynthesis inhibitors (data pooled from $n = 2–5$ experiments, two to three replicates per experiment). Statistical differences were calculated using one-way ANOVA and Sidak test. $P < 0.05$ was considered statistically significant. *, $P < 0.05$; **, $P < 0.01$. ***, $P < 0.001$; n.s., not significant. chx, cycloheximide.

To directly determine whether biosynthetic activity is responsible for cell lethality under arid conditions, we exposed control- and serum-treated cancer cells to several small-molecule inhibitors of biosynthesis, including a CDK4/6 inhibitor (abemaciclib), mTOR inhibitors (rapamycin and Torin1), and a protein synthesis inhibitor (cycloheximide). We observed that these inhibitors reduced both proliferation (**Fig. 7C**) and cell death (**Fig. 7D**). Together, these results suggest that biosynthesis and proliferation in the absence of adequate resources reduces the viability of metabolically deprived cancer cells.

Discussion

Metabolic vulnerabilities of hypoxic, nutrient-deprived pancreatic cancer cells

It is well-established that the tumor microenvironment differs proximal and distal to blood vessels, with hypoxia being increased distally and associated with poorly perfused, slowly cycling cells. While studies of interstitial tumor fluid metabolites and other media formulations approximating physiologic conditions have been instructive (36, 63, 64), these studies are unable to resolve differences between well perfused versus hypoxic, poorly perfused tumor regions. It is increasingly recognized that standard cell culture conditions, which have been optimized to promote cell proliferation at 20% oxygen, differ considerably from the hypoxic and nutrient-deprived tumor microenvironments that dominate most solid tumors *in vivo* (10). Previous investigations have deprived cancer cells of single or pairs of nutrients (13, 14, 16, 65, 66) conditions that are unlikely to mimic nutrient availability in poorly perfused tumor regions. Central to our efforts to recapitulate the poorly perfused, hypoxic microenvironment, we have identified a cell culture system that deprives cancer cells of multiple nutrients, resulting in slow cycling cells. The findings with our cell culture system were corroborated by studies using TIFM (36).

The "arid condition" used in this study was able to induce and maintain a stable and persistent slow-cycling state by depriving cells of the full spectrum of metabolites and oxygen, mimicking the poorly perfused tumor microenvironment. Using this experimental system, we found that two broadly delineated cellular states in solid tumors – a rapidly cycling state characterized by metabolic sufficiency and a slow-cycling, scavenger-like state driven by nutrient and oxygen deprivation – manifest markedly different dependencies. Rapidly cycling cells are sensitive to gemcitabine, as expected, while slow-cycling cells are chemoresistant. As such, uncovering the metabolic vulnerabilities of these slow-cycling cells using an unbiased gRNA CRISPR/Cas-9 screening would be foundational for novel therapeutic strategies.

Cancer cells cultured in the arid condition experienced extensive transcriptional rewiring, conferring resistance to treatments targeting biosynthesis or proliferation and, at the same time, generating dependencies on pathways that are not as important in rapidly cycling, glycolytic cells. Intriguingly, we found that slow-cycling cancer cells following nutrient and oxygen deprivation exhibited an unforeseen dependency on OXPHOS, surprising given prior evidence suggesting that cancer cells can have a reduced dependency on OXPHOS in low-glucose conditions (13) or hypoxia (16, 65). These observations highlight the value of an experimental system in which multiple nutrients are withdrawn simultaneously. Importantly, the preclinical success of agents that target OXPHOS might reflect the increased sensitivity of tumors, like PDAC, that are metabolically deprived *in vivo* (47–49, 67).

Adaptation to nutrient-deprived conditions engages various mechanisms for acquiring or repurposing metabolic resources to support survival, including autophagy, macropinocytosis, and anaplerosis (68). Meanwhile, cells reduce energy expenditure to avoid exhaustion (46, 69) or loss of homeostasis (70, 71). Consistent with this hypothesis, we found that promoting biosynthesis and proliferation under metabolically deprived conditions, by depletion of cell growth inhibitors, such as loss of TSC2, or repletion of serum, resulted in loss of fitness and cell death. Taken together, these observations reinforce the conclusion that reactivating cell growth programs hinders the survival of slow-cycling cells in nutrient deprived, hypoxic microenvironments.

Bcl-xL promotes the survival of slow-cycling tumor cells following nutrient deprivation

The observation that gRNAs directed at Bcl-xL were among the top ones selectively depleted in arid conditions was not

unexpected given its role as an inhibitor of apoptosis (52). However, Bcl-xL was not redundant with other Bcl2 family members following nutrient deprivation (72–74). Notably, Bcl-xL suppresses cell-cycle progression, a property that correlates with its prosurvival effects (53). Efforts to decouple the cell-cycle and survival function have yielded conflicting results (53, 75, 76). In this study, we found that depletion of Bcl-xL promotes both cell-cycle progression and cell death within the same cancer cell population under arid conditions. Furthermore, pharmacologic inhibition of CDK4/6, mTOR, or protein synthesis relieved the dependency on Bcl-xL under arid conditions. This suggests that at least under our arid conditions, Bcl-xL is causally related to its quiescent function under nutrient-deprived conditions.

While Bcl-xL has been extensively studied *in vitro,* less is known about its function *in vivo* and it is mainly studied for its antiapoptotic function (77). Here, we provide evidence that Bcl-xL functions in poorly perfused regions and maintains tumor cell quiescence that may be essential for preserving this chemoresistant population. Concordantly, Bcl-xL KO PDAC tumors grow slower, despite the increased drive for biosynthesis (phospo-S6) and proliferation (Ki67/EdU), a result that is in agreement with the paradoxical response observed in PDAC tumors treated with rapamycin (68). The finding that Bcl-xL expression is enriched in slow-cycling cancer cells in human PDAC suggests that the relationships between metabolic microenvironments and survival programs reported here are conserved in human tumors.

The Bcl2 family of apoptosis inhibitors has been the focus of considerable attention over the years as potential targets for cancer therapy, but the majority of preclinical studies and clinical trials testing Bcl2 family inhibitors as monotherapy have shown limited efficacy in solid tumors (78). Consistent with these findings, pharmacologic inhibition of Bcl-xL with the inhibitor A-1331852 had only a modest effect on tumor growth *in vivo*. In contrast, we found that this drug markedly enhanced the activity of standard-of-care gemcitabine/nab-paclitaxel, a synergy likely due to complementary effects on chemoresistant cells in poorly perfused tumor regions and chemo-sensitive cells in well perfused tumor regions although we cannot exclude enhancements of gemcitabine killing in well-perfused regions due to loss of control of apoptosis as an additional factor. These observations establish the potential of combining treatments that target both the rapidly and slowly cycling subsets of cancer cells, as treatments eliminating either subset alone are insufficient (2).

Authors' Disclosures

Authors' Contributions

Y. Sela: Conceptualization, data curation, formal analysis, validation, investigation, writing–original draft, writing–review and editing. **J. Li:** Conceptualization, data curation, formal analysis, validation, visualization, writing–original draft, writing–review and editing. **S. Maheswaran:** Investigation, writing–review and editing. **R. Norgard:** Formal analysis, investigation, writing–review and editing. **S. Yuan:** Formal analysis, investigation, writing–review and editing. **M. Hubbi:** Investigation, writing–review and editing. **M. Doepner:** Investigation, writing–review and editing. **J.P. Xu:** Investigation. **E.S. Ho:** Investigation, writing–review and editing. **C. Mesaros:** Resources, investigation, visualization, writing–review and editing. **C. Sheehan:** Resources, methodology. **G. Croley:** Resources, methodology. **A. Muir:** Resources, methodology, writing–review and editing. **I.A. Blair:** Data curation, supervision, investigation, writing–review and editing. **O. Shalem:** Resources, methodology, writing–review and editing. **C.V. Dang:** Resources, supervision, methodology, writing–original draft, writing–review and editing. **B.Z. Stanger:** Conceptualization, resources, supervision, funding acquisition, writing–original draft, writing–review and editing.

Acknowledgments

References

1. Sahin AA, Ro JY, El-Naggar AK, Wilson PL, Teague K, Blick M, et al. Tumor proliferative fraction in solid malignant neoplasms: a comparative study of Ki-67 immunostaining and flow cytometric determinations. Am J Clin Pathol 1991;96: 512–9.

2. Yano S, Zhang Y, Miwa S, Tome Y, Hiroshima Y, Uehara F, et al. Spatial-temporal FUCCI imaging of each cell in a tumor demonstrates locational dependence of cell cycle dynamics and chemoresponsiveness. Cell Cycle 2014;13:2110–9.

3. Granada AE, Jiménez A, Stewart-Ornstein J, Blüthgena N, Reber S, Jambhekar A, et al. The effects of proliferation status and cell cycle phase on the responses of single cells to chemotherapy. Mol Biol Cell 2020;31:845–57.

4. Rossari F, Zucchinetti C, Buda G, Orciuolo E. Tumor dormancy as an alternative step in the development of chemoresistance and metastasis - clinical implications. Cell Oncol 2020;43:155–76.

5. Pinto B, Henriques AC, Silva PMA, Bousbaa H. Three-dimensional spheroids as in vitro preclinical models for cancer research. Pharmaceutics 2020;12:1–38.

6. Porschen R, Classen S, Piontek M, Borchard F. Vascularization of carcinomas of the esophagus and its correlation with tumor proliferation. Cancer Res 1994;54: 587–91.

7. Bartlett R, Everett W, Lim S, Natasha G, Loizidou M, Jell G, et al. Personalized in vitro cancer modeling — Fantasy or reality? Transl Oncol 2014;7: 657–64.

8. Kumar S, Sharife H, Kreisel T, Mogilevsky M, Bar-Lev L, Grunewald M, et al. Intra-tumoral metabolic zonation and resultant phenotypic diversification are dictated by blood vessel proximity. Cell Metab 2019;30:201–11.

9. Kyle AH, Baker JHE, Minchinton AI. Targeting quiescent tumor cells via oxygen and IGF-I supplementation. Cancer Res 2012;72:801–9.

10. Mayers JR, Vander Heiden MG. Famine versus feast: Understanding the metabolism of tumors in vivo. Trends Biochem Sci 2015;40:130–40.

11. Nik Nabil WN, Xi Z, Song Z, Jin L, Zhang XD, Zhou H, et al. Towards a framework for better understanding of quiescent cancer cells. Cells 2021; 10:562.

12. Jain IH, Calvo SE, Markhard AL, Skinner OS, To TL, Ast T, et al. Genetic screen for cell fitness in high or low oxygen highlights mitochondrial and lipid metabolism. Cell 2020;181:716–27.

13. Birsoy K, Possemato R, Lorbeer FK, Bayraktar EC, Thiru P, Yucel B, et al. Metabolic determinants of cancer cell sensitivity to glucose limitation and biguanides. Nature 2014;508:108–12.

14. Keenan MM, Liu B, Tang X, Wu J, Cyr D, Stevens RD, et al. ACLY and ACC1 regulate hypoxia-induced apoptosis by modulating ETV4 via α-ketoglutarate. PLoS Genet 2015;11:1–29.

15. Yoshino S, Hara T, Weng JS, Takahashi Y, Seiki M, Sakamoto T. Genetic screening of new genes responsible for cellular adaptation to hypoxia using a genome-wide shRNA library. PLoS One 2012;7:e35590.

16. Thomas LW, Esposito C, Morgan RE, Price S, Young J, Williams SP, et al. Genome-wide CRISPR/Cas9 deletion screen defines mitochondrial gene essentiality and identifies routes for tumour cell viability in hypoxia. Commun Biol 2021;4:1–12.

17. Li J, Byrne KT, Yan F, Yamazoe T, Chen Z, Baslan T, et al. Tumor cell-intrinsic factors underlie heterogeneity of immune cell infiltration and response to immunotherapy. Immunity 2018;49:178–93.

18. Doench JG, Root D. Optimized sgRNA design to maximize activity and minimize off-target effects of CRISPR-Cas9 Synthesis of an arrayed sgRNA library targeting the human genome. Nat Biotechnol 2016;34:184–91.

19. Shalem O, Sanjana NE, Hartenian E, Shi X, Scott DA, Heckl D, et al. Shalem et al., 2014. Science 2014;343:84–7.

20. Guo L, Worth AJ, Mesaros C, Snyder NW, Jerry D, Blair IA. Diisopropylethylamine/hexafluoroisopropanol-mediated ion- pairing UHPLC-MS for phosphate and carboxylate metabolite analysis: utility for studying cellular metabolism. Rapid Commun Mass Spectrom 2016;30:1835–45.

21. Grant GD, Kedziora KM, Limas JC, Cook JG, Purvis JE. Accurate delineation of cell cycle phase transitions in living cells with PIP-FUCCI. Cell Cycle 2018;17:2496–516.

22. Tarumoto Y, Lu B, Somerville TDD, Huang YH, Milazzo JP, Wu XS, et al. LKB1, salt-inducible kinases, and MEF2C are linked dependencies in acute myeloid leukemia. Mol Cell 2018;69:1017–27.

23. Walter DM, Venancio OS, Buza EL, Tobias JW, Deshpande C, Gudiel A, et al. Systematic in vivo inactivation of chromatin- regulating enzymes identifies Setd2 as a potent tumor suppressor in lung adenocarcinoma. Cancer Res 2017;77:1719–29.

24. Shi J, Wang E, Milazzo JP, Wang Z, Kinney JB, Vakoc CR. 2015.14. Nat Biotechnol 2015;33:661–7.

25. N'Diaye EN, Kajihara KK, Hsieh I, Morisaki H, Debnath J, Brown EJ. PLIC proteins or ubiquilins regulate autophagy-dependent cell survival during nutrient starvation. EMBO Rep 2009;10:173–9.

26. Love MI, Huber W, Anders S. Moderated estimation of fold change and dispersion for RNA-seq data with DESeq2. Genome Biol 2014;15:1–21.

27. Győrffy B. Survival analysis across the entire transcriptome identifies biomarkers with the highest prognostic power in breast cancer. Comput Struct Biotechnol J 2021;19:4101–9.

28. Olive KP, Jacobetz MA, Davidson CJ, Gopinathan A, McIntyre D, Honess D, et al. Inhibition of Hedgehog signaling enhances delivery of chemotherapy in a mouse model of pancreatic cancer. Science 2009;324:1457–61.

29. Koong AC, Mehta VK, Le QT, Fisher GA, Terris DJ, Brown JM, et al. Pancreatic tumors show high levels of hypoxia. Int J Radiat Oncol Biol Phys 2000;48:919–22.

30. Kamphorst JJ, Nofal M, Commisso C, Hackett SR, Lu W, Grabocka E, et al. Human pancreatic cancer tumors are nutrient poor and tumor cells actively scavenge extracellular protein. Cancer Res 2015;75:544–53.

31. Lee KE, Spata M, Bayne LJ, Buza EL, Durham AC, Allman D, et al. Hif1a deletion reveals pro-neoplastic function of B cells in pancreatic neoplasia. Cancer Discov 2016;6:256–69.

32. Aiello NM, Bajor DL, Norgard RJ, Sahmoud A, Bhagwat N, Pham MN, et al. Metastatic progression is associated with dynamic changes in the local microenvironment. Nat Commun 2016;7:12819.

33. Aeffner F, Martin NT, Peljto M, Black JC, Major JK, Jangani M, et al. Quantitative assessment of pancreatic cancer precursor lesions in IHC-stained tissue with a tissue image analysis platform. Lab Investig 2016;96:1327–36.

34. Ströbel P, Ellenrieder V, Maisonneuve P, Neesse A. Stromal features of the primary tumor are not pancreatic cancer. Cells 2019;9:1–13.

35. Ferrara C, Tessari G, Poletti A, Giacon C, Meggiato T, Martines D, et al. Ki-67 and c-jun expression in pancreatic cancer: a prognostic marker? Oncol Rep 1999;6:1117–39.

36. Sullivan MR, Danai LV, Lewis CA, Chan SH, Gui DY, Kunchok T, et al. Quantification of microenvironmental metabolites in murine cancers reveals determinants of tumor nutrient availability. Elife 2019;8:1–27.

37. Zaidi M, Fu F, Cojocari D, McKee TD, Wouters BG. Quantitative visualization of hypoxia and proliferation gradients within histological tissue sections. Front Bioeng Biotechnol 2019;7:1–9.

38. Commisso C, Davidson SM, Soydaner-Azeloglu RG, Parker SJ, Kamphorst JJ, Hackett S, et al. Macropinocytosis of protein is an amino acid supply route in Ras-transformed cells. Nature 2013;497:633–7.

39. Yang A, Herter-Sprie G, Zhang H, Lin EY, Biancur D, Wang X, et al. Autophagy sustains pancreatic cancer growth through both cell-autonomous and nonautonomous mechanisms. Cancer Discov 2018;8:276–87.

40. Gameiro PA, Struhl K. Nutrient deprivation elicits a transcriptional and translational inflammatory response coupled to decreased protein synthesis. Cell Rep 2018;24:1415–24.

41. Awasthi N, Zhang C, Schwarz AM, Hinz S, Wang C, Williams NS, et al. Comparative benefits of nab-paclitaxel over gemcitabine or polysorbate-based docetaxel in experimental pancreatic cancer. Carcinogenesis 2013;34:2361–9.

42. Huggett MT, Tudzarova S, Proctor I, Loddo M, Keane MG, Stoeber K, et al. Cdc7 is a potent anti-cancer target in pancreatic cancer due to abrogation of the DNA origin activation checkpoint. Oncotarget 2016;7:18495–507.

43. Cencic R, Carrier M, Galicia-Vázquez G, Bordeleau ME, Sukarieh R, Bourdeau A, et al. Antitumor activity and mechanism of action of the cyclopenta[b]benzofuran, silvestrol. PLoS One 2009;4:e5223.

44. Zachar Z, Marecek J, Maturo C, Gupta S, Stuart SD, Howell K, et al. Non-redox-active lipoate derivates disrupt cancer cell mitochondrial metabolism and are potent anticancer agents in vivo. J Mol Med 2011;89:1137–48.

45. Zhong Y, Li X, Yu D, Li X, Li Y, Long Y, et al. Application of mitochondrial pyruvate carrier blocker UK5099 creates metabolic reprogram and greater stem-like properties in LnCap prostate cancer cells in vitro. Oncotarget 2015;6:37758–69.

46. Liu L, Cash TP, Jones RG, Keith B, Thompson CB, Simon MC. Hypoxia-induced energy stress regulates mRNA translation and cell growth. Mol Cell 2006;21:521–31.

47. Rajeshkumar NV, Yabuuchi S, Pai SG, De OE, Hidalgo M, Maitra A, et al. Treatment of pancreatic cancer patient – derived xenograft panel with metabolic inhibitors reveals Ef fi cacy of phenformin. Clin Cancer Res 2017;23:5639–48.

48. Masoud R, Reyes-Castellanos G, Lac S, Garcia J, Dou S, Shintu L, et al. Targeting mitochondrial complex I overcomes chemoresistance in high OXPHOS pancreatic cancer. Cell Reports Med 2020;1:100143.

49. Lee KC, Maturo C, Perera CN, Luddy J, Rodriguez R, Shorr R. Translational assessment of mitochondrial dysfunction of pancreatic cancer from in vitro gene microarray and animal efficacy studies, to early clinical studies, via the novel tumor-specific anti-mitochondrial agent, CPI-613. Ann Transl Med 2014;2:1–10.

50. Philip PA, Buyse ME, Alistar AT, Lima CM, Luther S, Pardee TS, et al. A phase III open-label trial to evaluate efficacy and safety of CPI-613 plus modified FOLFIRINOX (mFFX) versus FOLFIRINOX (FFX) in patients with metastatic adenocarcinoma of the pancreas. Futur Oncol 2019;15:3189–96.

51. Boise LH, González-García M, Postema CE, Ding L, Lindsten T, Turka LA, et al. Bcl-X, a Bcl-2-related gene that functions as a dominant regulator of apoptotic cell death. Cell 1993;74:597–608.

52. Michels J, Kepp O, Senovilla L, Lissa D, Castedo M, Kroemer G, et al. Functions of BCL-XL at the interface between cell death and metabolism. Int J Cell Biol 2013;2013:705294.

53. Janumyan YM, Sansam CG, Chattopadhyay A, Cheng N, Soucie EL, Penn LZ, et al. Bcl-xL/Bcl-2 coordinately regulates apoptosis, cell cycle arrest and cell cycle entry. EMBO J 2003;22:5459–70.

54. Janumyan Y, Cui Q, Yan L, Sansam CG, Valentin M, Yang E. G0 function of BCL2 and BCL-xL requires BAX, BAK, and p27 phosphorylation by mirk, revealing a novel role of BAX and BAK in quiescence regulation. J Biol Chem 2008;283:34108–20.

55. Tao ZF, Hasvold L, Wang L, Wang X, Petros AM, Park CH, et al. Discovery of a potent and selective BCL-XLinhibitor with in vivo activity. ACS Med Chem Lett 2014;5:1088–93.

56. Ducreux M, Seufferlein T, Van Laethem JL, Laurent-Puig P, Smolenschi C, Malka D, et al. Systemic treatment of pancreatic cancer revisited. Semin Oncol 2019;46:28–38.

57. Leverson JD, Phillips DC, Mitten MJ, Boghaert ER, Diaz D, Tahir SK, et al. Exploiting selective BCL-2 family inhibitors to dissect cell survival dependencies and define improved strategies for cancer therapy. Sci Transl Med 2015;7:1–12.

58. Kahn BM, Lucas A, Alur RG, Wengyn MD, Schwartz GW, Li J, et al. The vascular landscape of human cancer. J Clin Invest 2021;131:1–16.

59. Peng J, Sun BF, Chen CY, Zhou JY, Chen YS, Chen H, Sabatini DM. Single-cell RNA-seq highlights intra-tumoral heterogeneity and malignant progression in pancreatic ductal adenocarcinoma. Cell Res 2019;29:725–38.

60. Steele NG, Carpenter ES, Kemp SB, Sirihorachai V, The S, Delrosario L, et al. HHS Public Access. Nat Cancer 2021;1:1097–112.

61. Lin W, Noel P, Borazanci EH, Lee J, Amini A, Han IW, et al. Single-cell transcriptome analysis of tumor and stromal compartments of pancreatic ductal adenocarcinoma primary tumors and metastatic lesions. Genome Med 2020;12:80.

62. Linette GP, Li Y, Roth K, Korsmeyer SJ. Cross talk between cell death and cell cycle progression: BCL-2 regulates NFAT-mediated activation. Proc Natl Acad Sci U S A 1996;93:9545–52.

63. Rossiter NJ, Huggler KS, Adelmann CH, Keys HR, Soens RW, Sabatini DM, et al. CRISPR screens in physiologic medium reveal conditionally essential genes in human cells. Cell Metab 2021;33:1248–63.

64. Vande Voorde J, Ackermann T, Pfetzer N, Sumpton D, Mackay G, Kalna G, et al. Improving the metabolic fidelity of cancer models with a physiological cell culture medium. Sci Adv 2019;5:eaau7314.

65. Jain IH, Calvo SE, Markhard AL, Skinner OS, To T, Ast T, et al. HHS Public Access. Cell 2021;181:716–27.

66. Bao MHR, Yang C, Tse APW, Wei L, Lee D, Zhang MS, et al. Genome-wide CRISPR-Cas9 knockout library screening identified PTPMT1 in cardiolipin synthesis is crucial to survival in hypoxia in liver cancer. Cell Rep 2021;34:108676.

67. Zhang X, Fryknäs M, Hernlund E, Fayad W, De Milito A, Olofsson MH, et al. Induction of mitochondrial dysfunction as a strategy for targeting tumour cells in metabolically compromised microenvironments. Nat Commun 2014;5:3295.

68. Palm W, Park Y, Wright K, Pavlova NN, Tuveson DA, Thompson CB. The utilization of extracellular proteins as nutrients is suppressed by mTORC1. Cell 2015;162:259–70.

69. Hardie DG. AMP-activated protein kinase-an energy sensor that regulates all aspects of cell function. Genes Dev 2011;25:1895–908.

70. Young RM, Ackerman D, Quinn ZL, Mancuso A, Gruber M, Liu L, et al. Dysregulated mTORC1 renders cells critically dependent on desaturated lipids for survival under tumor-like stress. Genes Dev 2013;27:1115–31.

71. Maddocks ODK, Berkers CR, Mason SM, Zheng L, Blyth K, Gottlieb E, et al. Serine starvation induces stress and p53 dependent metabolic remodeling in cancer cells. Nature 2019;493:542–6.

72. Eno CO, Zhao G, Olberding KE, Li C. The Bcl-2 proteins Noxa and Bcl-xL co-ordinately regulate oxidative stress-induced apoptosis. Biochem J 2012; 444:69–78.

73. Eichhorn JM, Alford SE, Sakurikar N, Chambers TC. Molecular analysis of functional redundancy among anti-apoptotic Bcl-2 proteins and its role in cancer cell survival. Exp Cell Res 2014;322:415–24.

74. Hatch H, Dolinski BM, Nguyen T, Harmonay L, Al-Assaad AS, Ayers M, et al. MCL1 and BCL-xL levels in solid tumors are predictive of dinaciclib-induced apoptosis. PLoS One 2014;9:e108371.

75. Huang DCS, O'Reilly LA, Strasser A, Cory S. The anti-apoptosis function of: Bcl-2 can be genetically separated from its inhibitory effect on cell cycle entry. EMBO J 1997;16:4628–38.

76. Bonnefoy-Berard N, Aouacheria A, Verschelde C, Quemeneur L, Marçais A, Marvel J. Control of proliferation by Bcl-2 family members. Biochim Biophys Acta 2004;1644:159–68.

77. D'Aguanno S, Del Bufalo D. Inhibition of anti-apoptotic Bcl-2 proteins in preclinical and clinical studies: current overview in cancer. Cells 2020;9:1287.

78. Merino D, Kelly GL, Lessene G, Wei AH, Roberts AW, Strasser A. BH3-mimetic drugs: blazing the trail for new cancer medicines. Cancer Cell 2018;34:879–91.